

1
2
3
4
5
6
7
8
9
10
11
12
13
14
15
16
17
18
19
20
21
22
23

Revision 1:

In-situ U-Th/Pb geochronology of (urano)thorite

John M. Cottle¹

1) Department of Earth Science, University of California, Santa Barbara, California

93106-9630, USA (e-mail: cottle@geol.ucsb.edu)

Abstract

A Laser-Ablation-Multi-Collector-Inductively Coupled Plasma Mass Spectrometry (LA-MC-ICPMS) study of seven thorite and uranothorite [(Th,U)SiO₄] samples ranging in age from ~13 to ~500 Ma provides new insights into the U-Th/Pb isotope systematics of these geologically significant, high-Th mineral species. Despite extreme actinide enrichment and complex intra-crystal zonation in actinides and rare earth elements, this study demonstrates that radiogenic-lead loss and/or metamictization is minimal and restricted to domains that have undergone significant hydration. Dating of four igneous uranothorites yields ages that are concordant in U/Pb and Th/Pb space, consistent with other high-temperature chronometers, and are inferred to accurately reflect the timing of crystallization of each rock. Similarly, Th/Pb ages of three thorite and/or huttonite-bearing samples yield geologically plausible dates consistent with other mineral chronometers. No evidence of isotopic inheritance was observed in any of the samples. Data presented here demonstrate for the first time the feasibility of extracting accurate and precise U/Pb and Th/Pb ages from Phanerozoic thorite, uranothorite and huttonite using LA-MC-ICPMS at the 5µm spatial resolution. These phases have the potential to be robust chronometers in igneous and metamorphic rocks as well as to provide

24 important provenance information complementary to more widely used minerals such as
25 detrital zircon.

26

27 **Keywords:** *Thorite, Uranothorite, Huttonite, Laser Ablation, Geochronology*

28

29 **Introduction**

30 The tetragonal orthosilicate thorite [ThSiO₄] and its monoclinic polymorph huttonite
31 occur in a wide variety of geological environments ranging from (but not restricted to)
32 felsic igneous rocks (Parrish and Tirrul, 1989, Hetherington and Harlov, 2008),
33 metasediments (e.g. Speer, 1982), base metal ore deposits (e.g. Ifill et al., 1989) and fault
34 zones (Kamineni and Lemire, 1991). Thorite may be either primary, or form by the
35 breakdown of other Th-rich minerals such as allanite, monazite or zircon (Hetherington
36 and Harlov, 2008). Its variable occurrence, combined with an ability to accommodate
37 large amounts of U and Th within its structure makes it a potentially useful chronometer
38 to quantify the timing and duration of a diverse range of geological events.

39 In pursuit of this goal there have been several attempts to date (urano)thorite using either
40 Electron probe microanalyzer (EPMA) (Parslow et al., 1985; Enami et al., 1993; Förster
41 et al., 2000; Jercinovic et al., 2002; Cocherie and Legendre, 2007) or Thermal Ionization
42 Mass Spectrometry (ID-TIMS) (e.g. Henjes-Kunst, et al., 1988; Parrish and Tirrul, 1989;
43 von Blanckenburg, 1992). The former method has generally met with limited success,
44 which these authors attribute to thorite's often metamict state and its susceptibility to
45 hydration and associated radiogenic lead loss. ID-TIMS has been used in at least two
46 published studies. Parrish and Tirrul (1989) analyzed uranothorite along with zircon and
47 monazite in monzogranite from the Karakoram granite in northern Pakistan (see below
48 for further details). They obtained three nearly concordant zircon analyses and two
49 duplicate fractions of uranothorite that together yielded a mean U/Pb age of 21.0 ± 0.5
50 Ma. Monazites from the same rock were reversely discordant with ages ranging between
51 17 and 19 Ma which Parrish and Tirrul (1989) postulated was the result of slow cooling,

52 persistence of high temperatures following crystallization, and partial lead loss in
53 monazite, none of which apparently affected the thorite.

54 Von Blanckenburg (1992) analyzed allanite, sphene, apatite and thorite from a
55 granodiorite of the Central Alpine Bergell intrusion (central Europe). They argued that
56 both the allanite and sphene lacked inheritance and were magmatic in origin. The mean
57 age of the allanite and sphene (30.12 ± 0.17 Ma) was interpreted as the timing of
58 granodiorite intrusion. A single grain thorite fraction yielded a concordant U/Pb age of
59 28.36 Ma and Th/Pb age of 27.6 Ma. The younger thorite U/Pb age relative to the allanite
60 – sphene age was inferred to be a result of recrystallization and the ~3% discrepancy
61 between U/Pb and Th/Pb ages of the thorite resulted from Th gain, U loss, or ^{208}Pb loss
62 from strongly ^{232}Th -enriched domains (Von Blanckenburg, 1992).

63 These two isotopic studies highlight the possibility of obtaining U/Pb and/or Th/Pb dates
64 from (urano)thorite. However, significant questions still remain about the interpretation
65 of (urano)thorite dates relative to other high temperature chronometers such as zircon,
66 monazite, sphene and allanite. The cause and significance of the disequilibrium between
67 the Th/Pb and U/Pb systems in thorite identified by Von Blanckenburg (1992) also
68 remains unresolved. In addition, although often described as occurring within clastic
69 sediments, the utility of (urano)thorite and huttonite as indicators of sedimentary
70 provenance remains untested.

71 In this contribution, the U/Pb and Th/Pb isotope systematics of (urano)thorite and
72 huttonite are explored by combining EPMA elemental mapping with recently developed
73 in-situ Laser Ablation micro-sampling techniques, which allow simultaneous acquisition
74 of U, Th, and Pb isotopes from small volumes of ablated material. The method employed

75 here (Laser-Ablation-Multi-Collector- Inductively Coupled Plasma Mass Spectrometry,
76 LA-MC-ICPMS) affords high spatial resolution (~5 μm diameter pits) and enables the
77 chemistry and morphology of a grain to be directly related to its isotopic age.

78 The majority of U/Pb and Th/Pb data presented here are concordant, with no evidence of
79 disequilibrium between isotope systems. Alteration and associated radiogenic lead-loss is
80 volumetrically minor and restricted to obviously altered domains. Dates obtained from
81 igneous uranothorite are consistent with other high temperature chronometers (e.g.
82 zircon), whereas detrital thorite and huttonite yield complementary information about
83 geologic source regions not recorded by detrital zircon from the same sample.

84

85

Sample Descriptions

86 Geologically well-constrained samples were chosen for this study, including three
87 samples for which complementary geochronological data already exists (See Table 1 for
88 summary of samples analyzed). Further, five of the samples (M33, AD41, H4, H8 and
89 P68787) have similar chemistry and petrogenetic origin, enabling more direct inter-
90 sample comparisons on the behavior of Th-rich minerals formed during crustal anatexis.

91

92

M33

93 Sample M33 is from the high-grade Mogok Metamorphic Belt (MMB), an arcuate zone
94 that extends from the eastern Himalayan syntaxis in the north, through the Indo–Burman
95 Ranges to the Andaman Sea in the south. The geological setting and tectonic significance
96 of M33 is discussed in detail by Searle et al. (2007) and described briefly here. M33 is an
97 undeformed quartz + plagioclase + K-feldspar + biotite granite dike with a weak flow

98 banding fabric, collected from Belin Quarry in the central Burmese part of the MMB
99 (Searle et al. 2007, their Figs. 4 and 5b; Table 1). Accessory phases are dominated by
100 zircon, apatite and uranothorite. Petrological data suggest that this is an S-type
101 leucogranite that formed by muscovite dehydration melting of a mid-crustal pelitic
102 assemblage following crustal thickening associated with the collision of India and Asia
103 (Searle et al., 2007). A single grain concordant ID-TIMS zircon fraction yielded a
104 $^{206}\text{Pb}/^{238}\text{U}$ date of 53.1 ± 0.2 Ma and a single grain thorite has a $^{207}\text{Pb}/^{235}\text{U}$ age of $54.1 \pm$
105 0.1 Ma. In addition, seven U/Pb LA-MC-ICPMS spot analyses on uranothorite,
106 normalized to primary reference material Manangotry monazite yield a $^{206}\text{Pb}/^{238}\text{U}$ -
107 $^{207}\text{Pb}*/^{235}\text{U}$ concordia age of 59.5 ± 0.9 Ma, (MSWD of concordance = 0.97). The
108 authors inferred the ~6 Ma discrepancy between the ID-TIMS and LA-MC-ICPMS ages
109 to reflect Pb-loss in both ID-TIMS zircon and thorite fractions and concluded that the
110 $^{207}\text{Pb}*/^{235}\text{U}$ LA-MC-ICPMS thorite concordia age of 59.5 ± 0.9 Ma provided the best
111 estimate of the magmatic crystallization age of M33 (Searle et al., 2007, their Figure 8g).
112 This sample was selected for its well-constrained geologic context and available U/Pb
113 ID-TIMS and LA-MC-ICPMS data for both zircon and uranothorite (Searle et al., 2007).

114

115

AD41

116 AD41 is a migmatitic augen gneiss from a section of the Greater Himalayan series (GHS)
117 crops out on the east side of the Phung Chu river in the Kharta valley of south Tibet
118 (Cottle et al., 2009a, their Figs. 2 and 4b; Table 1). The GHS in this region is a 30-km-
119 thick sequence of metamorphic and anatectic rocks that form the high-grade core of the
120 orogen. Sample AD41 is a distinctly banded, mylonitic augen gneiss with a well-

121 developed foliation defined by laths of biotite and fibrolite. The restitic portion of the
122 rock is composed of biotite, sillimanite, quartz, plagioclase and K-feldspar, while the cm-
123 thick, syn-kinematic leucogranitic leucosomes comprise aggregates of K-feldspar, quartz
124 and rare biotite. Accessory phases are dominated by zircon, apatite and uranothorite, with
125 the latter restricted to the leucosomes. The leucosomes are interpreted to have formed as
126 a result of in-situ partial melting of the host meta-granitoid (Cottle et al., 2009a). U/Pb
127 dating of zircons from AD41 yield an age of 440 ± 6 Ma, interpreted as the crystallization
128 age of the protolith granitoid (Cottle et al., 2009a). This age is comparable to other
129 gneisses within the GHS in the Everest region some ~60 km to the east, e.g. the Namche
130 orthogneiss (Viskupic and Hodges, 2001). Eight U/Pb LA-ICPMS analyses of
131 uranothorite (normalized to a primary reference Manangotry monazite) yielded a mean
132 $^{206}\text{Pb}/^{238}\text{U}$ date of 15.8 ± 0.2 Ma (MSWD 0.9, n=8) (Cottle et al. 2009a their Fig. 7f).

133

134

H4 and H8

135 Sample H4 is an S-type monzogranite from the south side of the Baltoro Glacier Valley,
136 eight km NNW of Masherbrum peak in the Karakoram region of northern Pakistan.
137 Sample H8 is a megacrystic K-feldspar granite collected from 3 km NW of Bialo peak
138 (Parrish and Tirrul, 1989 their Fig. 1; Table 1). Both samples are from the Baltoro
139 granite, part of the Cretaceous–Miocene composite Karokoram Batholith of the northwest
140 Himalaya (Parrish and Tirrul 1989; and references therein). The geology and accessory
141 phase geochronology of H4 and H8 is described by Parrish and Tirrul (1989) and
142 references therein. Zircon data for H8 are all highly discordant with $^{207}\text{Pb}/^{206}\text{Pb}$ apparent
143 dates ranging from 635 Ma to 1750 Ma. One uranothorite fraction is reversely discordant

144 with an inferred date of ~16.5 Ma, whereas monazites are ~18 Ma. Two fractions of
145 uranothorite (a total of six crystals) from H4 yield an ID-TIMS $^{206}\text{Pb}/^{238}\text{U}$ age of $21.3 \pm$
146 0.1 Ma (U ~10300ppm, Pb ~990 ppm, Pb $^{206}\text{Pb}/^{238}\text{U} = 0.0033 \pm 0.3\%$, $^{207}\text{Pb}/^{206}\text{Pb} =$
147 $0.0463 \pm 0.4\%$, $^{208}\text{Pb}/^{232}\text{Th} = 0.00104 \pm 0.5\%$, Parrish and Turrill 1989). These
148 geologically well-constrained samples were selected for further analysis because of the
149 published U/Pb ID-TIMS ages for H4 derived from uranothorite and zircon and
150 monazite. For this study uranothorite was picked from the same mineral separates used
151 by Parrish and Turrill (1989).

152

153

P68787

154 P68787 is a coarse-grained equigranular hornblende monzodiorite from the Hunt Glacier
155 in the Dry Valleys region of Antarctica (from the Geological and Nuclear Science,
156 Dunedin, New Zealand Collection, kindly provided by A. Tulloch). This sample is part of
157 the Granite Harbor Intrusives, an extensive suite of dominantly calc-alkaline mid-crustal
158 magmatic rocks formed during the Neoproterozoic–Ordovician Ross orogeny. Zircon
159 from this sample has a mean $^{206}\text{Pb}/^{238}\text{U}$ LA-MC-ICPMS date of 502.1 ± 2.6 Ma (Hagen-
160 Peter et al. 2011; Table 1). For this study uranothorite was picked from the same heavy
161 mineral separate as used by Hagen-Peter et al. (2011).

162

163

OU-16321

164 OU-16321 from the University of Otago, Dunedin, New Zealand Collection is from a 1-
165 to 2-cm-thick carbonate-rich vein containing, in approximate order of abundance, ferroan
166 dolomite, magnesian dolomite, apatite, albite, reddish-brown thorite crystals up to 2-mm-

167 long, and Nb-rutile (Table 1, White, 1962; Cooper, 1971). This rock comes from Gout
168 Creek, Haast River, in the South Island of New Zealand and occurs as part of a
169 lamprohyric dike-swarm with carbonatitic affinities. Previous geochronology on
170 associated rocks yields U/Pb primary magmatic crystallization zircon ages ranging from
171 24.6 – 24.1 Ma (Cooper et al., 1986).

172

173

Gillespie's Beach ThSiO₄

174 Thorite, huttonite, zircon and rutile were extracted from a heavy mineral concentrate
175 collected from Gillespie's Beach, on the West coast of the South Island, New Zealand.
176 The heavy mineral concentrate is dominated by magnetite but also contains minor
177 amounts of scheelite, zircon, thorite, huttonite, rutile, and apatite. Thorite from
178 Gillespie's Beach occurs in brown and green varieties while huttonite was distinguished
179 from thorite primarily by x-ray diffraction (XRD). Gillespie's Beach is significant
180 because it is the type locality for huttonite originally described in detail by Pabst and
181 Hutton (1951). Förster et al. (2006) used the EPMA total U-Th/Pb method to obtain
182 Miocene dates for huttonite and dates ranging from late Triassic–early Jurassic to early
183 Tertiary for thorite (Table 1).

184

185

Methods

186 Uranothorites were separated using standard crushing, heavy liquid, and isodynamic
187 magnetic separation techniques. A representative crystal from each sample was subjected
188 to XRD to confirm whether it was tetragonal thorite or a Th-silicate dimorph, e.g.
189 huttonite (monoclinic [(Th,U)SiO₄]). Although only weak thorite diffraction patterns were

190 generated, they confirm that each crystal has a tetragonal crystal system with average (*n*
191 = 8) unit cell dimensions: $a = b = 7.18$ (3) Å $c = 6.09$ (4) Å, $a:c = 1: 0.848$ and a cell
192 volume of $v = 314$ Å³ (calculated from Unit Cell).

193 Grains representative of the variation in population morphology were handpicked
194 in ethanol and mounted in one-inch diameter epoxy resin discs, polished to reveal
195 equatorial sections, then carbon-coated. To elucidate zonation and/or alteration patterns,
196 identify inclusions within grains, and to aid positioning of spots for later isotope analysis
197 such that multiple domains/or altered areas were avoided, backscattered electron (BSE)
198 maps were produced using a FEI Quanta400F scanning electron microscope (SEM). In
199 addition, elemental maps of U, Th, Y and P were made using a Cameca SX-100 EPMA
200 housed at the University of California, Santa Barbara (UCSB). Quantitative major and
201 trace element analyses were performed using the same EPMA. Detailed EPMA analytical
202 methods are presented in Appendix 1 and data are presented in Table 2.

203 After EPMA mapping and analysis, U, Th, and Pb isotopes were collected from
204 carefully selected sites using a LA-MC-ICPMS housed at UCSB. Analytical methods
205 follow Cottle et al. (2012, 2013) and Kylander-Clark et al. (2013). A detailed analytical
206 method is presented in Appendix 1 and data are presented in Table 3 (uranothorite),
207 Table 4 (thorite and huttonite) and Table 5 (detrital zircon). For thorites, the ‘H4’
208 uranothorite (Parrish and Tirrul, 1989) served as the matrix-matched primary reference
209 material (RM) to monitor and correct for mass bias, as well as Pb/U and Pb/Th down-
210 hole fractionation (see below for further detail on matrix-matching). No Pb/Th age data
211 exist for H4 (or any of the samples analyzed in this study), therefore for normalization
212 purposes, the Pb/Th and Pb/U systems for H4 were assumed to be concordant. Since no

213 secondary thorite RM currently exists, two zircon reference materials ('91500' and 'GJ-
214 1') were analyzed concurrently as an external monitor of instrument performance. For
215 zircon analyses, '91500' (1062.4 ± 0.4 Ma $^{206}\text{Pb}/^{238}\text{U}$ ID-TIMS age, Wiedenbeck et al.
216 1995) was employed as the primary RM. To monitor data accuracy, a secondary
217 reference zircon 'GJ-1' (608.5 ± 0.4 Ma $^{207}\text{Pb}/^{206}\text{Pb}$ ID-TIMS age, Jackson et al. 2004)
218 was analyzed concurrently (once every seven unknowns) yielding a weighted mean
219 $^{206}\text{Pb}/^{238}\text{U}$ age of 600.5 ± 1.6 , MSWD = 1.5, n = 28. Data reduction, including corrections
220 for baseline, instrumental drift, mass bias, down-hole fractionation as well as age
221 calculations were carried out using Iolite v. 2.1.2 (Paton et al. 2010). Background
222 intensities and changes in instrumental bias were interpolated using a smoothed cubic
223 spline while down-hole inter-element fractionation was modeled using an exponential
224 function. Statistics for baselines, on peak intensities and isotopic ratios were calculated
225 using the mean with a 2.S.D. outlier rejection. Concordia and weighted mean date plots
226 were calculated in Isoplot v.3 (Ludwig 2003) using the ^{238}U and ^{235}U decay constants of
227 Steiger and Jäger, (1977) and the ^{232}Th decay constant of Amelin and Zaitsev (2002). All
228 uncertainties in data tables and concordia plots are quoted at the 2σ confidence level.

229

230

Results

231

(urano)thorite morphology and zoning

232 Igneous (urano)thorite in this study are generally doubly-terminated, euhedral to
233 subhedral, green to brown translucent crystals that range from short 2:1 (length:width
234 aspect ratio) to elongate (5:1). Integrating information from U, Th, Y, and P x-ray maps
235 and BSE images (Figs. 1 and 2) reveals a variety of internal structures, zoning and

236 alteration patterns. Many samples show one or more generations of cusped-lobate or
237 crosscutting flame and tongue structures (e.g. M33, AD41, Gillespie huttonite and thorite,
238 Fig. 1). These crystals have a patchy appearance in BSE, suggestive of multiple episodes
239 of intra-crystal dissolution, re-precipitation and/or intergrowth and amalgamation of
240 smaller grains.

241 Less commonly, samples show either minimal internal zoning in U, Th, Y, or P
242 (e.g. H4, H8, Fig. 1) or have oscillatory zoning (e.g. P68787, Fig. 1) analogous to
243 textures observed in igneous zircon. Relict oscillatory zoning subsequently overprinted
244 by recrystallization textures is occasionally preserved in brown thorites from the
245 Gillespie's Beach sample (Fig. 1). In the Gillespie's Beach sample, crystals typically
246 display minor patchy zoning in Th, U, P, and Y but also contain numerous inclusions of
247 xenotime (red spots in P and Y maps) along with minor, and much smaller, apatite and
248 monazite.

249 In addition to alteration, many of the grains examined from each sample contain
250 inclusions of zircon (Fig. 2a). Intergrowths of these two minerals were not observed and
251 in most cases the thorite appears to have nucleated around zircon. Less common
252 inclusions of quartz, K-feldspar, allanite and xenotime were also observed (Fig. 2b).

253

254

Alteration

255 All grains display some degree of alteration, and this potentially has significant impacts
256 on the isotopic age of (part of) a crystal. Optically, some crystals contain visible orange
257 discoloration zones. In BSE, this is manifested as either thin (1-20 μm) (H4 and H8) or
258 discontinuous (in M33 and AD41) rims (Fig. 1, 2c, 2d). In all cases, the altered domain is

259 darker in BSE, lower in Th, Si, Pb and U and higher in P, Ca, Fe, Y and (OH, calculated
260 from stoichiometry) suggesting that these regions have probably undergone hydrous
261 alteration to thorogummite [(Th,U)(SiO₄)_{1-x} (OH)_{4x}].

262 Alteration occurs as irregular domains along cracks adjacent to fractures, at the
263 contact with inclusions, and as large internal portions of the grain. A particularly good
264 example of internal alteration occurs in a crystal from M33 (Fig. 1 and Fig. 2b). This
265 crystal shows an alteration zone that is darker in BSE, lower in U, Th and Pb and higher
266 in Y and P than the rest of the grain. The altered zone contains inclusions of high Th and
267 U (1.5 wt % ThO₂ and 1.3 wt% UO₂) xenotime (the red spots in the Y and P maps). In
268 addition, although the alteration zone itself (as defined by the higher Y + P domain) is
269 associated with a significant depletion in U, the area immediately surrounding the
270 alteration is enriched in U relative to the unaltered portion of the crystal (Fig. 2b)
271 suggesting some decoupling of U and Th. Another form of alteration locally occurs in
272 many of the samples, but is best illustrated in sample OU16321. Crystals typically
273 display minor patchy zoning in Th, U, P and Y and contain numerous inclusions of
274 xenotime (red spots in P and Y maps) along with minor, and much smaller, apatite and
275 monazite (Fig. 1).

276

277

Mineral Chemistry

278 The chemistry of the investigated uranothorites is relatively consistent both within and
279 between samples (Table 2). Thorium is the dominant cation (52.1 – 57.8 wt% ThO₂),
280 with lesser amounts of U (18.5 – 26.2 wt % UO₂), Si (16.1 – 17.4 wt% SiO₂), P (0.4 – 1.4

281 wt% P₂O₅) and Y (0.4 – 1.9 wt% Y₂O₃) and Pb (0.3 – 0.5 wt% PbO). Thorites have more
282 Th, P, Y, and REE and less U than uranothorites.

283 For the unaltered domains, totals are consistently ~96–98% with cation
284 proportions in approximately the correct stoichiometry for ThSiO₄. Totals less than 100%
285 for thorite are commonly reported in the literature and, as outlined in detail by Förster
286 (2006), may potentially be related to one or more of: 1) the presence of absorbed
287 molecular water or hydroxyl substituted for silica; 2) the presence of elements not
288 included in the analytical routine; and 3) presence of uranium^(VI) oxide.

289 Because of their thin and irregular nature, only a few altered regions of crystals in
290 M33, AD41, H4 and H8 could confidentially be targeted with the EPMA (Table 2).
291 Analytical totals (~77 – 88%) are much lower than the pristine domains, suggesting that
292 these domains may contain a significant proportion of OH. This issue notwithstanding,
293 altered domains tend to be lower in U, Th, Pb and Fe and higher in Si, Ca, P and
294 occasionally REE.

295

296 **U-Th/Pb Isotope data**

297 **Matrix-matched reference material for LA-ICPMS**

298 During LA-ICPMS isotopic analysis a major source of uncertainty is the time-dependent
299 fractionation of elements as a result of the ablation process. Fractionation, defined as the
300 change in measured element (isotope) ratio signals with time (Fryer et al., 1995), is a poorly
301 understood process. However, for a given set of analytical conditions, fractionation occurs as
302 a result of differential vaporization and mobilization of ablated particles. Of particular
303 importance to this study is Laser-Induced Elemental Fractionation (LIEF), a well-
304 documented effect observed in previous U-Th/Pb geochronologic studies (e.g. Hirata and

305 Nesbitt, 1995; Horn et al., 2000; Kosler et al., 2001, Paton et al., 2010). The degree of LIEF
306 is controlled by the way the laser interacts with the sample (absorption characteristics) as
307 well as the sample's chemical composition. The net result is that geologic materials with
308 different structural properties and chemical compositions produce substantially different
309 time-dependent fractionation profiles. The majority of LA-ICPMS geochronologic studies
310 that employ a static spot (rather than a dynamic raster) use a sample-standard bracket
311 approach and assume that sample and reference material fractionate in a similar manner.
312 Therefore, any difference in time-dependent fractionation profile between sample and
313 primary reference material potentially leads to introduction of considerable uncertainty into
314 the analysis.

315 No well-characterized (urano)thorite LA-ICPMS reference material currently
316 exists, therefore in this study a series of experiments were conducted to assess if a similar
317 framework matrix (e.g. XSiO_4 such as zircon) or a matrix with a similar actinide content
318 (e.g. a high-Th phase such as monazite) could be employed to accurately correct for LIEF
319 in (urano)thorite, or if a matrix-matched reference material is necessary to generate
320 accurate data in static spot mode.

321 Three uranothorites along with Manangotry monazite [552.9 Ma $^{206}\text{Pb}/^{238}\text{U}$, 554
322 Ma $^{207}\text{Pb}/^{206}\text{Pb}$ ID-TIMS ages, (Horstwood et al., 2003)], Plešovice zircon [337.13 \pm 0.37
323 Ma $^{206}\text{Pb}/^{238}\text{U}$ ID-TIMS age, (Sláma et al., 2008)] and NIST SRM610 glass were
324 analyzed. So as not to saturate the secondary electron multipliers, a relatively small static
325 spot size (5 μm diameter pit) and low fluence (1.2 J/cm²) was employed. H4 data was
326 normalized to the ID-TIMS values of Parrish and Turrill (1989). The reference ages of
327 M33 and AD41 were taken from Searle et al. (2007) and Cottle et al. (2009a),
328 respectively. As outlined below, the age of AD41 reported by Cottle et al. (2009a) may

329 be inaccurate by as much as 10%, however this level of uncertainty has negligible affect
330 on the shape and position of the curves in Figure 3. Each sample was inferred to be
331 concordant in U/Pb and Th/Pb space and Th/Pb normalization values were derived from
332 U/Pb data.

333 Figure 3 shows exponential curves fitted to the mean of 10 repeat static spot
334 ablations of the various samples. In both U/Pb and Th/Pb space, the uranothorites have a
335 very similar fractionation trend, implying they ablate in a very similar manner. However,
336 this trend is significantly different from monazite, zircon, or NIST610. In U/Pb space, the
337 monazite and zircon have a much lower degree of fractionation while NIST610 has a
338 negative fractionation slope. In Th/Pb space the monazite, zircon, and NIST610 all have
339 significantly different fractionation slopes. It is clear from Figure 3 that a matrix-matched
340 reference material is necessary to accurately model and correct for $^{206}\text{Pb}/^{238}\text{U}$ and/or
341 $^{208}\text{Pb}/^{232}\text{Th}$ fractionation in the unknowns when a static spot is employed. Based on this
342 conclusion, the $^{206}\text{Pb}/^{238}\text{U}$ and/or $^{208}\text{Pb}/^{232}\text{Th}$ (urano)thorite and huttonite data presented
343 below are all normalized to H4 as the concurrently analyzed primary reference material.

344

345

M33

346 For this study, an additional 25 LA-MC-ICPMS spot analyses were carried out on
347 uranothorite grains from the same mineral separate as Searle et al. (2007). Twenty-two of
348 the analyses are concordant in U/Pb and Th/Pb space yielding a weighted mean
349 $^{206}\text{Pb}/^{238}\text{U}$ date of 54.0 ± 0.4 Ma (MSWD 0.8), and a weighted mean $^{208}\text{Pb}/^{232}\text{Th}$ date of
350 53.9 ± 0.5 Ma (MSWD 1.3) (Fig. 4A-B, Table 3). Three additional analyses deliberately
351 placed over altered domains yield younger apparent $^{206}\text{Pb}/^{238}\text{U}$ and $^{208}\text{Pb}/^{232}\text{Th}$ dates of

352 ~48 Ma, consistent with radiogenic lead loss.

353

354

AD41

355 Forty-one new analyses from six grains were collected as part of this study, with forty
356 analyses yielding a weighted mean $^{206}\text{Pb}/^{238}\text{U}$ date of 14.8 ± 0.1 (MSWD 1.9) and a
357 weighted mean $^{208}\text{Pb}/^{232}\text{Th}$ date of 13.5 ± 0.1 (MSWD 3.7) (Fig. 4 C-D, Table 3). One
358 spot deliberately placed over an altered domain gives an apparent date of ~11 Ma.

359

360

H8

361 Thirty-five analyses conducted during this study yield a weighted mean $^{206}\text{Pb}/^{238}\text{U}$ date of
362 22.1 ± 0.2 Ma (MSWD 2.7), and a weighted mean $^{208}\text{Pb}/^{232}\text{Th}$ date of 21.4 ± 0.1 Ma
363 (MSWD 1.7) (Fig. 4E-F, Table 3). Two additional analyses deliberately placed over
364 altered domains yield younger apparent dates of ~18.5-20 Ma, consistent with radiogenic
365 lead loss.

366

367

P68787

368 Ten analyses from five grains yield a weighted mean $^{206}\text{Pb}/^{238}\text{U}$ date of 495 ± 6 Ma
369 (MSWD 1.2), and a weighted mean $^{208}\text{Pb}/^{232}\text{Th}$ date of 492 ± 8 Ma (MSWD 1.4) (Fig.
370 4G-H, Table 3). One analysis was rejected as it contains a significant amount of
371 common-lead, likely from partial ablation of an inclusion.

372

373

OU-16321

374 Twelve analyses from five grains yield a weighted mean $^{208}\text{Pb}/^{232}\text{Th}$ date of 19.7 ± 0.4
375 Ma (MSWD 1.5). A single analysis on an altered domain gives an apparent date of ~ 17
376 Ma (Fig. 5, Table 4). The number of analyses is relatively small since only areas that
377 were determined to be free of (the numerous) xenotime inclusions were measured.

378

379

Gillespie's Beach ThSiO_4 and Zircon

380 Analysis of 75 individual crystals of brown thorite from the Gillespie's Beach mineral
381 separate yield consistent dates of ~ 75 Ma (Fig. 6, Table 4). Although not strictly valid for
382 detrital samples, taking a weighted mean $^{208}\text{Pb}/^{232}\text{Th}$ date gives 74.7 ± 0.4 Ma (MSWD
383 1.4). The MSWD of near unity indicates the possibility that these crystals were sourced
384 from a rock or suite of rocks with a single age population. Analyses of 79 individual
385 crystals of green thorite yield $^{208}\text{Pb}/^{232}\text{Th}$ dates ranging from 210 Ma to 23 Ma with a
386 prominent age peak at ~ 75 Ma (Fig. 6, Table 4). Analysis of five huttonite grains yields
387 dates ranging from 17 to 12 Ma (Fig. 6, Table 4). These dates are broadly similar to total
388 U-Th/Pb ages obtained by Förster et al. (2000) using the EPMA. Analysis of 100 detrital
389 zircons from the same mineral separate yields age peaks at ~ 260 Ma, ~ 380 Ma, ~ 480 -
390 550 Ma, $\sim 620 - 680$ Ma and a minor component of Proterozoic and Achaean ages (Fig.
391 7, Table 5).

392

393

Discussion

394

Mineral Chemistry and Alteration

395 The first key observation from the detailed x-ray imaging carried out in this study is that
396 the vast majority of both thorite and uranothorite crystals are internally zoned in both

397 major (U, Th) and trace (Y, P, REE) elements. Intra-crystalline zoning takes multiple
398 forms, but is commonly manifested as patchy textures that are consistent with one or
399 more episodes of fluid-mediated intra-crystal dissolution, re-precipitation and/or
400 intergrowth and amalgamation of smaller grains. Such textures have previously been
401 described from other minerals such as apatite (e.g. Harlov et al. 2005), monazite and
402 xenotime (e.g. Harlov et al., 2010, 2011; Hetherington et al., 2010, Williams et al., 2011)
403 and are commonly interpreted as the result of a fluid-mediated dissolution/re-
404 precipitation reaction. That formation of these textures is a common process in
405 (urano)thorites is also supported by only rare preservation of crystals from igneous rocks
406 that preserve ‘igneous’ textures such as oscillatory zoning.

407 Altered rims and intra-crystalline domains yield ages that are consistent with loss
408 of radiogenic Pb, with ages from altered domains typically ~11 – 15% younger than
409 pristine domains from the same samples. This radiogenic Pb-loss is consistent with the
410 results of experimental alteration studies of other phases such as monazite that have been
411 subjected to dissolution/re-precipitation processes (e.g. Seydoux-Guillaume et al., 2002;
412 Williams et al., 2011). In contrast, and despite complex intra-crystal zoning patterns, U-
413 Th/Pb geochronologic data retrieved for pristine domains in these samples is relatively
414 simple (see further discussion below) yielding single populations with no clear evidence
415 for disturbance in the U-Th/Pb isotope systems or multiple geologic events. It is clear that
416 in the studied samples, complex major and trace element zonation does not correlate to
417 age-differences, as commonly observed in other minerals such as monazite (e.g. Foster et
418 al., 2002).

419

420

Geochronology

421 Two samples, M33 and AD41, were analyzed by LA-ICPMS static spot analyses in
422 previous studies. In both cases, these data were normalized to Manangotry reference
423 monazite. However, given the matrix-effects associated with static spot analyses
424 identified in this work (Fig. 3), it is expected that these data are inaccurate. The
425 inaccuracy, which in this case is on the order of 10%, arises because the time-dependent
426 (down-hole) slope of the inter-element ratio(s) of the primary reference material is less
427 than that of the unknown. This leads to an under-correction of the down-hole
428 fractionation, which in turn results in an age that is apparently too old. This is further
429 supported by the observation that the Searle et al. (2007) LA-ICPMS date for M33
430 uranothorite (59.5 Ma) is ~10% too old compared to both the new LA-ICPMS data (54.0
431 Ma) presented here and the single ID-TIMS datum (~54 Ma) of Searle et al. (2007) (the
432 difference between LA-ICPMS and ID-TIMS data was previously interpreted by Searle
433 as Pb-loss in the ID-TIMS fraction).

434 There are no independent age constraints on the uranothorite from AD41, but the
435 existing AD41 date (15.8 Ma normalized to Manangotry reference monazite, Cottle et al.,
436 2009a) is also ~10% too old compared to the data (14.8 Ma) presented here, suggesting a
437 similar level of inaccuracy in the original data. These two samples illustrate the
438 importance of utilizing a matrix-matched reference material in order to produce accurate
439 LA-ICPMS (urano)thorite dates using a static spot, and that failing to do so results in
440 inaccuracies of at least 10% relative to the true age.

441

442

Concordance

443 Uranothorite analyzed in this study are consistently concordant in U/Pb space, both
444 within crystals (multiple spots on the same crystal) and between crystals in the same
445 rock. This has two key implications for the geochronology of uranothorite: 1) the lack of
446 ‘reverse discordance’ suggests that both U decay chains have achieved secular
447 equilibrium and that there has been no gain of intermediate decay products such as ^{230}Th
448 and/or ^{231}Pa ; 2) the lack of discordance in the U/Pb system in pristine crystal domains
449 strongly suggests that there as been minimal radiogenic Pb-loss and; 3) there is no
450 correlation between U/Pb dates and either crystal size or position within the crystal
451 suggesting no resolvable volume diffusion of daughter products. Thus, in contrast to the
452 work of von Blanckenburg (1992), uranothorites in this study have remained closed to U
453 and its decay products throughout their history and can be treated as a reliable high
454 temperature chronometer.

455 For thorite and huttonite only Th/Pb isotope ratios were measured, so there is no
456 test of concordance. However, the dated thorite and huttonite produce geologically
457 reasonable dates (see below) implying that there has been no gain or loss of parent,
458 intermediate or daughter isotopes in the ^{232}Th decay chain and therefore these minerals
459 also serve as useful chronometers.

460 In his pioneering work on reverse discordance in monazite, Schärer (1984 p.191)
461 stated that “*U-Pb ages of Th-rich minerals such as monazite (and allanite) have to be*
462 *corrected for excess ^{206}Pb due to excess ^{230}Th ... the extent of this correction depends on*
463 *the degree of Th-U fractionation and on the age of the rock.*”. Minerals such as monazite
464 strongly partition Th into their structure during crystallization and include significant and
465 variable amounts of ^{230}Th along with ^{232}Th such that the Th/U ratio of the monazite is

466 much greater than that of the magma from which it crystallized. ^{230}Th is an intermediate
467 daughter product of ^{238}U that decays to “unsupported” ^{206}Pb (e.g. Schärer 1984), resulting
468 in apparent $^{206}\text{Pb}/^{238}\text{U}$ ages that are reversely discordant or “too-old” with respect to
469 $^{207}\text{Pb}/^{235}\text{U}$ and $^{208}\text{Pb}/^{232}\text{Th}$ ages. The degree of excess ^{206}Pb can be significant, for
470 example Cottle et al. (2009) documented ~12 Ma Himalayan monazite with $^{206}\text{Pb}/^{238}\text{U}$
471 ages up to 50% older than $^{207}\text{Pb}/^{235}\text{U}$ ages (for a constant $^{208}\text{Pb}/^{232}\text{Th}$ ratio).

472 In contrast to the common observation of ‘excess ^{206}Pb ’ in monazite, no reverse
473 discordance was observed in uranothorite analyzed in this study. This has two
474 fundamental implications for uranothorite geochronology. Firstly, the $^{206}\text{Pb}/^{238}\text{U}$ dates
475 obtained from uranothorite can be considered as reliable as either $^{207}\text{Pb}/^{235}\text{U}$ or
476 $^{208}\text{Pb}/^{232}\text{Th}$ ages. Secondly, since there is no apparent Th/U disequilibrium between the
477 uranothorite and the magma/fluid from which it crystallized. The Th/U ratio of the
478 uranothorite is therefore a good approximation of the bulk rock from which it
479 crystallized. In other words, the U and Th bulk rock / uranothorite partition co-efficient is
480 approximately 1. The latter is consistent with the observation of Parrish and Tirrul
481 (1989).

482

483 **Comparison to other chronometers**

484 Geochronology data exists from other accessory phases for three of the dated samples
485 (M33, H8 and P68787), thus offering the opportunity to compare (urano)thorite dates to
486 other mineral chronometers. M33 uranothorite (54.0 ± 0.4 Ma $^{206}\text{Pb}/^{238}\text{U}$ date and $53.9 \pm$
487 0.5 Ma $^{208}\text{Pb}/^{232}\text{Th}$ date) is within uncertainty of both ID-TIMS zircon (53.1 ± 0.2 Ma)
488 and uranothorite (54.1 ± 0.1 Ma) data of Searle et al., (2007). This suggests that the new

489 LA-ICPMS data are accurate with respect to the ID-TIMS thorite data and also consistent
490 with the existing zircon data. It seems reasonable to conclude that uranothorite from M33
491 can be confidently interpreted to accurately record the timing of igneous crystallization of
492 this leucogranite body. Uranothorite from H8 is equivalent to ID-TIMS uranothorite and
493 zircon from related rocks (e.g. H4 21.0 ± 0.5 Ma, Parrish and Tirrul, 1989) and is best
494 explained as recording the timing of magmatic crystallization of this sample. Zircons
495 from H8 are inherited, ranging in age from 635 Ma to 1750 Ma. In this rock, the
496 uranothorite (which does not show any sign of inheritance) provides as a robust record of
497 igneous crystallization whereas the zircon does not.

498 Uranothorite from P68787 (495 ± 6 Ma $^{206}\text{Pb}/^{238}\text{U}$ date and 492 ± 8 Ma
499 $^{208}\text{Pb}/^{232}\text{Th}$ date) lies well within uncertainty of zircon (502 ± 2.6 Ma, Hagen-Peter et al.
500 2011) from the same mineral separate, again suggesting that the uranothorite accurately
501 records crystallization of this igneous rock. Although this is a relatively small dataset
502 from which to compare, in each case the dated uranothorites yield ages that are consistent
503 with other high temperature chronometers such as zircon. This suggests that in igneous
504 rocks, uranothorite has the ability to accurately record the timing of melt crystallization
505 and is therefore of significant use, especially where zircon inheritance is prevalent.

506 The Gillespie's Beach detrital sample provides insight into the utility of thorite
507 and huttonite as provenance indicators. All brown thorite along with a significant portion
508 of the green thorites are essentially the same age at ~ 74 Ma (Fig. 6 and 7), implying that
509 these detrital crystals were derived from either a single lithologic source or from a suite
510 of rocks with a single-age population. The majority of green thorite analyses also yield
511 ~ 74 Ma dates, with a minor component of older, Cretaceous and Jurassic ages. In

512 contrast, huttonite yields ages ranging from 17 to 12 Ma. By comparison, detrital zircons
513 from the same mineral separate yields age peaks at ~260 Ma, ~380 Ma, ~480 - 550 Ma
514 and ~620 – 680 Ma.

515 All but one of the thorite analyses is significantly younger than the detrital zircons
516 analyzed from the same sample. The youngest concordant detrital zircon analysis ($223 \pm$
517 4.2 Ma) overlaps within error of the oldest (209.4 ± 12.1 Ma) green thorite analysis (Fig.
518 8) implying that detrital thorite and huttonite has the potential to record provenance
519 information that the zircon does not. In this case, taking the detrital zircon signature in
520 isolation would lead to the erroneous conclusion that the source region(s) for this sample
521 did not experience any significant tectonic event(s) post ~220 Ma.

522 Accurately tracing the origin of the thorite in the Gillespie's Beach sample is
523 somewhat difficult given the diverse geologic history of the West coast of the South
524 Island. One key observation is that the multiple ~74 Ma thorite ages overlap with U/Pb
525 zircon and monazite ages from pegmatite dikes (Chamberlain et al., 1995; Batt et al.,
526 1999) and the host Alpine schist (Mortimer and Cooper, 2004) cropping out immediately
527 to the east of the Alpine fault (Fig. 8). In the absence of other comparable ages, the
528 Alpine pegmatite dikes and/or the host schist represent a probable source. The 17 – 12
529 Ma Huttonite from the Gillespie's Beach sample can potentially be related to either fluid-
530 assisted alteration associated with emplacement of carbonatites and associated rocks in
531 the Alpine Dike swarm (Cooper et al., 1987) and/or younger metamorphism/alteration of
532 the Alpine schist associated with uplift along the Alpine fault (Batt et al., 1999). The
533 remaining minor Mesozoic component to the thorite age spectra could equally be related
534 to plutonic and/or metamorphic rocks west of the Alpine fault (Western Province) (Hiess

535 et al., 2010), or a detrital component in the sedimentary protolith to the Alpine schist
536 (Fig. 8, e.g. Campbell et al., 2007; Adams et al., 2013).

537

538 **Implications**

539 This study demonstrates that a matrix-matched reference material is essential in order to
540 produce accurate U-Th/Pb (urano)thorite static spot dates by LA-ICPMS. Neither an
541 [X]SiO₄ matrix such as zircon or a high-Th phase such as monazite behave in a similar
542 manner to (urano)thorite in terms of ablation characteristics, and specifically with respect
543 to LIEF. Using a matrix-matched reference uranothorite, samples analyzed in this study
544 yield concordant U/Pb and Th/Pb ages that are consistent with other high-temperature
545 chronometers. Uranothorite, unlike other high-Th phases such as monazite, does not
546 appear to suffer from disequilibrium in the ²³⁸U decay chain (i.e. ‘excess ²⁰⁶Pb’) such that
547 ²⁰⁶Pb/²³⁸U dates can be considered reliable. Radiogenic-lead loss and/or metamictization
548 appears to be minimal and restricted to domains that have undergone significant fluid-
549 assisted alteration and/or hydration. The lack of pervasive alteration and metamictization
550 makes (urano)thorite a robust chronometer in igneous and metamorphic rocks. Detrital
551 thorite and huttonite has the potential to record significant provenance information that
552 can elucidate a variety of igneous, metamorphic and alteration processes in the source
553 terrane(s).

554

555 **Acknowledgements**

556 Gareth Seward provided considerable assistance in obtaining EPMA data. Alan Cooper,
557 Bradley Hacker, Andy Tulloch, and Randy Parrish are thanked for providing samples

558 analyzed in this study. James Darling and Chris McFarlane provided insightful reviews
559 that significantly improved this manuscript. This material is based upon work supported
560 by the National Science Foundation under Grant No. (NSF-EAR-1050043).

561

562

Appendix – Analytical Methods

563 *XRD*: Single crystal x-ray diffraction (XRD) patterns were made with a Kappa Apex II x-
564 ray diffractometer in the Chemistry Department at the University of California, Santa
565 Barbara.

566

567 *EPMA*: elemental maps and quantitative major and trace element analyses were made
568 using a Cameca SX-100 Electron Probe MicroAnalyzer (EPMA) housed at the University
569 of California, Santa Barbara. x-ray maps of U (LPET, $M\alpha$), Th (LPET, $M\alpha$), Y (LTAP,
570 $L\alpha$), and P (LPET, $K\alpha$) were made in beam scan mode using 15 keV accelerating voltage,
571 200 nA beam current (equating to a $\sim 1 \mu\text{m}^3$ interaction volume), and a dwell time of 25
572 ms. Quantitative analyses were performed on the same instrument. Operating conditions
573 were 40 degrees takeoff angle, accelerating voltage of 20 keV, 200 nA beam current and
574 a beam diameter of 5 μm . Elements were acquired using analyzing crystals LLIF for La
575 $L\alpha$, Nd $L\alpha$, Pr $L\alpha$, Eu $L\alpha$, Gd $L\alpha$, Tb $L\alpha$, Dy $L\alpha$, Ho $L\alpha$, Er $L\alpha$, Tm $L\alpha$, Yb $L\alpha$, Lu $L\alpha$,
576 Fe $K\alpha$, Sm $L\alpha$, LPET for Pb $M\alpha$, U $M\alpha$, Ce $L\alpha$, Ca $K\alpha$, Y La , Th $M\alpha$, and TAP for P $K\alpha$,
577 Si $K\beta$, Al $K\alpha$.

578 The standards were ThO₂ for Th $M\alpha$, U-2 (10.00% UO₂ in diopside glass) for U
579 $M\alpha$, Anorthite (Grass Valley) U.C.#16706 for Al $K\alpha$, Diopside (Chesterman) for Si $K\beta$,
580 Ca $K\alpha$, Magnetite U.C. #3380 for Fe $K\alpha$, CePO₄ (USNM 168484) for Ce $L\alpha$, DyPO₄

581 (USNM 168485) for Dy $L\alpha$, ErPO₄ (USNM 168486) for Er $L\alpha$, EuPO₄ (USNM 168487)
582 for Eu $L\alpha$, GdPO₄ (USNM 168488) for Gd $L\alpha$, HoPO₄ (USNM 168489) for Ho $L\alpha$,
583 LaPO₄ (USNM 168490) for La $L\alpha$, P $K\alpha$, LuPO₄ (USNM 168491) for Lu $L\alpha$, NdPO₄
584 (USNM 168492) for Nd $L\alpha$, PrPO₄ (USNM 168493) for Pr $L\alpha$, SmPO₄ (USNM 168494)
585 for Sm $L\alpha$, TbPO₄ (USNM 168496) for Tb $L\alpha$, TmPO₄ (USNM 168497) for Tm $L\alpha$,
586 YbPO₄ (USNM 168498) for Yb $L\alpha$, YPO₄ (USNM 168499) for Y $L\alpha$, and Pyromorphite
587 (Cameca) for Pb $M\alpha$.

588 The counting time was 40 seconds for La $L\alpha$, Ce $L\alpha$, Nd $L\alpha$, Th ma , Pr $L\alpha$, Eu
589 $L\alpha$, Gd $L\alpha$, Tb $L\alpha$, Dy $L\alpha$, Ho $L\alpha$, Er $L\alpha$, Tm $L\alpha$, Yb $L\alpha$, Lu $L\alpha$, Fe $K\alpha$, Si $K\beta$, Sm $L\alpha$,
590 100 seconds for Al $K\alpha$, Pb $M\alpha$, 120 seconds for U $M\alpha$, 160 seconds for Y $L\alpha$, and 200
591 seconds for P $K\alpha$, Ca $K\alpha$. The off peak counting time was 40 seconds for La $L\alpha$, Ce $L\alpha$,
592 Nd $L\alpha$, Th $M\alpha$, Pr $L\alpha$, Eu $L\alpha$, Gd $L\alpha$, Tb $L\alpha$, Dy $L\alpha$, Ho $L\alpha$, Er $L\alpha$, Tm $L\alpha$, Yb $L\alpha$, Lu
593 $L\alpha$, Fe $K\alpha$, Si $K\beta$, Sm $L\alpha$, 100 seconds for Al $K\alpha$, Pb $M\alpha$, 120 seconds for U $M\alpha$, 160
594 seconds for Y $L\alpha$, and 200 seconds for P $K\alpha$, Ca $K\alpha$. Off Peak correction method was
595 Linear for La $L\alpha$, Ce $L\alpha$, Nd $L\alpha$, Th $M\alpha$, P $K\alpha$, Pr $L\alpha$, Gd $L\alpha$, Ho $L\alpha$, Tm $L\alpha$, Yb $L\alpha$, Si
596 $K\beta$, Ca $K\alpha$, Y $L\alpha$, Sm $L\alpha$, and Multi-Point for Lu $L\alpha$, Pb $M\alpha$, U $M\alpha$, Fe ka , Eu $L\alpha$, Al
597 $K\alpha$, Er la , Tb $L\alpha$, Dy $L\alpha$.

598 Unknown and standard intensities were corrected for deadtime. Standard
599 intensities were corrected for standard drift over time. Interference corrections were
600 applied to La for interference by Nd, and to Nd for interference by Ce, and to Pr for
601 interference by La, Y, and to Eu for interference by Nd, Pr, and to Gd for interference by
602 Nd, Ce, La, and to Dy for interference by Eu, and to Ho for interference by Gd, Lu, and
603 to Er for interference by Tb, and to Tm for interference by Dy, Gd, and to Yb for

604 interference by Eu, Dy, Tb, and to Lu for interference by Dy, Ho, and to Pb for
605 interference by Y, and to U for interference by Th, and to Fe for interference by Dy, and
606 to Al for interference by Tm, Yb, Th, and to Ca for interference by Pb and Yb. See
607 Donovan et al., (1993) for detail.

608 Oxygen was calculated by cation stoichiometry and included in the matrix
609 correction. The matrix correction method was ZAF or Phi-Rho-Z Calculations and the
610 mass absorption coefficients dataset was LINEMU Henke (LBL, 1985) < 10KeV /
611 CITZMU > 10KeV. The ZAF or Phi-Rho-Z algorithm utilized was Armstrong/Love
612 Scott (Armstrong, 1988). Accuracy of unknown analyses was checked routinely using in
613 house natural monazite reference materials, synthetic ThO₂ and NIST SRM 610.

614

615 *LA-MC-ICPMS*: In-situ U-Th/Pb geochronology analyses were performed using a laser
616 ablation multi-collector inductively coupled plasma mass spectrometer (LA-MC-ICPMS)
617 at the University of California Santa Barbara (UCSB). Analytical methods follow Cottle
618 et al. (2012, 2013); and Kylander-Clark et al. (2013) and are briefly described here.
619 Instrumentation consists of an Analyte 193 nm ArF excimer laser (Photon Machines, San
620 Diego, USA) equipped with a HelEx two-volume sample cell (Eggins et al., 1998)
621 attached to a Nu Plasma HR MC-ICPMS (Nu Instruments, Wrexham, UK). The collector
622 array on the Nu Plasma is configured to simultaneously measure ²³⁸U and ²³²Th on two
623 high-mass side Faraday cups and ²⁰⁸Pb, ²⁰⁷Pb, ²⁰⁶Pb, and ²⁰⁴X (where X includes ²⁰⁴Pb
624 and ²⁰⁴Hg) on four low-mass side secondary electron multipliers. Ablations were
625 conducted for 20 seconds each at 1.2 J/cm² or 1.5 J/cm² fluence (thorite, zircon), a
626 frequency of 4 Hz, and a pit diameter of 5µm or 20µm yielding craters ~3, or 9 µm deep

627 (as assessed by optical microscopy). Utilizing a sample–standard bracketing technique,
628 analyses of reference materials (RMs) with known isotopic composition were measured
629 before and after each set of seven unknown analyses. Data reduction, including
630 corrections for baseline, instrumental drift, mass bias, down-hole fractionation as well as
631 age calculations were carried out using Iolite v. 2.1.2 (Paton et al. 2010). Background
632 intensities and changes in instrumental bias were interpolated using a smoothed cubic
633 spline while down-hole inter-element fractionation was modeled using an exponential
634 function. Statistics for baselines, on peak intensities and isotopic ratios were calculated
635 using the mean with a 2.S.D. outlier rejection.

636

637

Figure Captions

638

639 **Figure 1.**

640 Representative Backscattered electron (BSE), Th, U, P, and Y x-ray Electron probe
641 microanalyzer (EPMA) maps of uranothorite (M33, AD41, H4, H8, P68787), thorite
642 (OU12321 and Gillespie Beach) and huttonite (Gillespie Beach) analyzed in this study.
643 Warmer colors are higher concentration relative to cooler colors. Scale bars are 50 μm .

644

645 **Figure 2.**

646 Representative Backscattered electron (BSE) images of typical alteration observed in this
647 study. A) inclusions of allanite and xenotime surrounded by altered uranothorite (sample
648 M33) (location of image is shown in Fig. 1). B) patchy recrystallization (sample AD41),
649 C) (H4) and D) (H8) altered rim surrounding pristine uranothorite. Scale bars are 25 μm .

650

651 **Figure 3.**

652 Self-normalized $^{206}\text{Pb}/^{238}\text{U}$ (A) and $^{208}\text{Pb}/^{232}\text{Th}$ (B) ratios as a function of time (depth)
653 during ablation. Each line is an exponential curve fitted to the mean of 10 static spot
654 ablations of each material (see Paton et al., 2010 for details of curve fitting). Thorites all
655 have similar slopes whereas monazite and NIST Glass have different slopes, illustrating
656 the need to use a matrix-matched reference material for thorite analysis in static spot
657 mode LA-ICPMS.

658

659 **Figure 4.**

660 Pb/U Concordia and weighted mean $^{208}\text{Pb}/^{232}\text{Th}$ plots for uranothorite samples. Analyses
661 in blue were specifically sited over altered domains, and are not considered in the final
662 age determinations.

663 A-B) M33. ID-TIMS data from Searle et al. (2007) plotted for comparison. C-D) AD-41.

664 E-F) H8. G-H) P68787. Mean LA-ICPMS $^{206}\text{Pb}/^{238}\text{U}$ zircon date (red ellipse) obtained by
665 Hagen-Peter et al. (2011) plotted for comparison.

666

667 **Figure 5.**

668 Weighted mean $^{208}\text{Pb}/^{232}\text{Th}$ plot for OU16321 thorite. Analysis in grey was rejected from
669 final date determination.

670

671 **Figure 6.**

672 Weighted mean $^{208}\text{Pb}/^{232}\text{Th}$ plot for Gillespie Beach thorite and huttonite. Although from

673 a detrital sample, brown thorite has a Mean Squared Weighted Deviates (MSWD) of 1.4,
674 consistent with a single age population. Photos of representative grains show a clear color
675 difference between ‘brown’ and ‘green’ thorite as well as dark green huttonite. Scale bars
676 are 200 μm .

677

678 **Figure 7.**

679 Kernel Density estimate for Gillespie Beach thorite, huttonite and zircon from the same
680 mineral separate. Only zircon <5% discordant are plotted. The majority of thorite is
681 younger than the zircon, with only very minor overlap between the oldest thorite and the
682 youngest detrital zircon.

683

684 **Figure 8.**

685 Summary diagram of existing geochronology data from major geologic units on the West
686 coast of the South Island of New Zealand. The ~ 74 Ma green and brown thorite
687 population overlaps with U/Pb monazite and zircon ages from both Alpine pegmatites
688 and Alpine schis. Oldest huttonites overlap in age with the Alpine dike swarm. Minor
689 older components to the green thorite population overlap with detrital zircon from both
690 the Eastern and Western provinces. Data sources: 1: This study; 2: Cooper et al. (1987);
691 3: Batt et al. (1999); 4: Chamberlain et al. (1995); 5: Mortimer and Cooper (2004); 6: Vry
692 et al.,(2004); 7: Hiess et al. (2010); 8: Campbell et al. (2007) and Adams et al. (2013).

693

694 **Table 1.**

695 Summary of samples analyzed in thus study. Mineral abbreviations after Whitney and

696 Evans (2010). References: 1: Searle et al. (2007); 2: Cottle et al. (2009a); 3: Parrish and
697 Tirrul (1989); 4: Hagen-Peter et al. (2011); 5: White (1962); 6: Cooper (1971); 7: Cooper
698 et al. (1987); 8: Pabst and Hutton (1951); 9: Förster et al. (2000).

699

700 **Table 2.**

701 Electron probe microanalyzer data table.

702

703 **Table 3.**

704 U-Th/Pb isotope data for uranothorite. Notes: a) concentration data are normalized to the
705 primary reference material and are accurate to approximately 10%, □b) $^{207}\text{Pb}/^{235}\text{U}$
706 calculated assuming a natural $^{238}\text{U}/^{235}\text{U}$ ratio of 137.88. c) Rho value is calculated
707 following the method outlined in Paton et al., (2010). □d) Age calculations are based on
708 the U decay constants of Steiger and Jäger (1977) and the Th decay constant of Amelin
709 and Zaitsev (2002). Isotopic ratios and ages are not corrected for common-Pb.

710

711 **Table 4.**

712 Th/Pb isotope data for thorite and huttonite. bdl: beyond detection limit. a) concentration
713 data are normalized to the primary reference material and are accurate to approximately
714 10%, □b) Age calculations are based on Th decay constant of Amelin and Zaitsev
715 (2002). Isotopic ratios and ages are not corrected for common-Pb.

716

717 **Table 5.**

718 U/Pb isotope data for detrital zircon from Gillespie's Beach. *indicates rejected datapoint
719 (>5% discordance). □a) concentration data□ are normalized to the primary reference
720 material and are accurate to approximately 10%. b) $^{207}\text{Pb}/^{235}\text{U}$ calculated assuming a
721 natural $^{235}\text{U}/^{238}\text{U}$ ratio of 137.88 c) Rho value is calculated following the method outlined
722 in Paton et al. (2010). □d) Age calculations are based on the U decay constants of Steiger
723 and Jäger (1977).
724

725

References

726 Amelin, Y., and Zaitsev, A.N. (2002) Precise geochronology of phoscorites and
727 carbonatites: the critical role of U-series disequilibrium in age interpretations.
728 *Geochimica et Cosmochimica Acta*. 66, 2399-2419.

729

730 Armstrong, J.T. (1988) Quantitative analysis of silicates and oxide minerals: Comparison
731 of Monte-Carlo, ZAF and Phi-Rho-Z procedures. In D.E. Newbwey Ed.,
732 *Microbeam Analysis*, p. 239-246. San Francisco Press, San Francisco.

733

734 Batt, G., Kohn, B.P., Braun, J., McDougall, I., and Ireland, T. (1999) New insight into the
735 dynamic development of the Southern Alps, New Zealand, from detailed
736 thermochronological investigation of the Mataketake Range pegmatites.
737 *Geological Society of London Special Publication*, 154, 261–282.

738

739 Adams, C. J., Mortimer, N., Campbell, H. J., and Griffin, W. L. (2013) Detrital zircon
740 geochronology and sandstone provenance of basement Waipapa Terrane
741 (Triassic–Cretaceous) and Cretaceous cover rocks (Northland Allochthon and
742 Houhora Complex) in northern North Island, New Zealand. *Geological Magazine*.
743 150, 89-109.

744

745 Chamberlain, C.P., Zeitler, P. K., and Cooper, A.F. (1995) Geochronologic constraints of
746 the uplift and metamorphism along the Alpine Fault, South Island, New Zealand.
747 *New Zealand Journal of Geology and Geophysics*, 38, 515–523.

748

749 Cocherie, A., and Legendre, O. (2007) Potential minerals for determining U-Th-Pb
750 chemical age using electron microprobe. *Lithos*, 93, 287-309.

751

752 Cooper, A.F. (1971) Carbonatites and fenitization associated with a lamprophyre dike-
753 swarm intrusive into schists of the New Zealand geosyncline. *Geological Society
754 of America Bulletin*, 82, 1327-1339.

755

756 Cooper, A.F. (1986) A carbonatitic lamprophyre dike swarm from the Southern Alps,
757 Otago and Westland. In I. E. M. Smith Ed., *Late Cenozoic Volcanism in New
758 Zealand*. Royal Society of New Zealand Bulletin, 23, 313-336.

759

760 Cooper, A.F., Barreiro, B.A., Kimbrough, D.L., and Mattinson, J.M. (1987)
761 Lamprophyre dike intrusion and the age of the Alpine Fault, New Zealand.
762 *Geology*, 15, 941-944.

763

764 Cottle, J.M., Jessup, M.J., Newell, D.L., Horstwood, M.S.A., Searle, M.P., Parrish, R.R.,
765 Waters, D.J., and Searle, M.P. (2009a) Geochronology of granulitized eclogite
766 from the Ama Drime Massif: implications for the tectonic evolution of the South
767 Tibetan Himalaya. *Tectonics*. 28, TC1002.

768

769 Cottle, J.M., Searle, M.P., Horstwood, M.S.A., and Waters, D.J. (2009b) Timing of Mid-
770 crustal metamorphism, melting and deformation in the Mt. Everest region of

771 southern Tibet revealed by U(-Th)-Pb geochronology. *Journal of Geology* 117,
772 643-664.

773

774 Cottle, J.M., Kylander-Clark, A.R.C., and Vrijmoed, J.C. (2012) U-Th/Pb
775 Geochronology of Detrital zircon and monazite by Single Shot Laser Ablation
776 Inductively Coupled Plasma Mass Spectrometry (SS-LA-ICPMS). *Chemical*
777 *Geology*, 332, 136-147.

778

779 Cottle, J.M., Burrows, A.J., Kylander-Clark, A., Freedman, P.A., and Cohen, R. (2013)
780 Enhanced sensitivity in laser ablation multi-collector inductively coupled plasma
781 mass spectrometry. *Journal of Analytical and Atomic Spectrometry*, 28, 1700-
782 1706.

783

784 Donovan, J.J., Snyder, D.A., and Rivers, M.L. (1993) An Improved Interference
785 Correction for Trace Element Analysis. *Microbeam Analysis*, 2, 23-28.

786

787 Eggins, S.M., Kinsley, L.P.J., and Shelley, J.M.G. (1998) Deposition and element
788 fractionation processes during atmospheric pressure laser sampling for analysis by
789 ICP-MS. *Applied Surface Science*, 127, 278–286.

790

791 Enami, M., Suzuki, K., Kingguo, Z., and Xiangshen Z. (1993) The chemical Th–U–total
792 Pb isochron ages of Jiaodong and Jiaonan metamorphic rocks in the Shandong
793 Peninsula, eastern China. *Island Arc*. 2, 104– 113.

794

795 Förster, H.-J., Harlov, D.E., and Milke, R. (2000) Composition and Th-U-total Pb ages of
796 huttonite and thorite from Gillespies Beach, South Island, New Zealand. Canadian
797 Mineralogist, 38, 675–684.

798

799 Foster, G., Gibson, H.D., Parrish, R.R., Horstwood, M.S.A., Fraser, J., and Tindle, A.
800 (2002) Textural, chemical and isotopic insights into the nature and behaviour of
801 metamorphic monazite. Chemical Geology, 191. 183-207.

802

803 Fryer, B.J., Jackson, S.E., and Longerich, H.P. (1995) The design, operation and role of
804 the laser ablation microprobe coupled with an inductively coupled plasma mass
805 spectrometer (LAM-ICP-MS) in the earth sciences. Canadian Mineralogist, 33,
806 303-312.

807

808 Hagen-Peter, G.A., Cottle, J.M., and Tulloch, A. (2011) Exploring the Petrochronology
809 of Subduction-Related Magmatism in the Ross Orogen: A Case Study from the
810 Dry Valleys, Southern Victoria Land, Antarctica. Geological Society of America
811 Abstracts with Programs, 43, 46.

812

813 Henjes-Kunst, F., Altherr, R., Kreuzer, H., and Tauber-Hansen, B. (1988) Disturbed U-
814 Th-Pb systematics of young zircons and uranorthorites: The case of the Miocene
815 Aegean granitoids (Greece). Chemical Geology, 73, 125-145.

816

- 817 Hetherington, C.J., and Harlov, D.E. (2008) Metasomatically induced formation of
818 thorite and uraninite inclusions in xenotime and monazite from granite
819 pegmatites, Hydra anorthosite massif, southwestern Norway: Mechanics and fluid
820 chemistry. *American Mineralogist*, 93, 806-820.
821
- 822 Hiess, J., Ireland, T., and Rattenbury, M. (2010) U-Th-Pb zircon and monazite
823 geochronology of Western Province gneissic rocks, central-south Westland, New
824 Zealand. *New Zealand Journal of Geology and Geophysics*, 53, 241-269.
825
- 826 Hirata, T., and Nesbitt, R.W. (1995) U-Pb isotope geology of zircon: Evaluation of the
827 laser probe-inductively coupled plasma mass spectrometry technique. *Geochimica
828 et Cosmochimica Acta*, 59, 2491-2500.
829
- 830 Horn I., Rudnick R., and McDonough W. (2000): Precise elemental and isotope ratio
831 determination by simultaneous solution nebulization and laser ablation-ICP-MS:
832 application to U-Pb geochronology. *Chemical Geology*, 167, 405-425.
833
- 834 Horstwood, M.S.A., Foster, G.L., Parrish, R.R., Noble, S.R., and Nowell, G.M. (2003)
835 Common-Pb corrected in situ U-Pb accessory mineral geochronology by LA-
836 MC-ICPMS. *Journal of Analytical and Atomic Spectrometry*, 18, 837-846.
837
- 838 Ifill, R.O., Clark, A.H., and Cooper, W.C. (1989) Mineralogical and process controls on
839 the oxidative acid-leaching of radioactive phases in Elliot Lake, Ontario, uranium

840 ores: I-uraninite, uranothorite, and monazite. *Canadian Mineralogical Journal*, 82,
841 65– 74.

842

843 Jackson, S.E., Pearson, N.J., Griffin, W.L., and Belousova, E.A. (2004) The application
844 of laser ablation-inductively coupled plasma-mass spectrometry to in situ U/Pb
845 zircon geochronology. *Chemical Geology*, 211, 47–69.

846

847 Jercinovic, M.J., Gillerman, V.S., and Stein, H.J. (2002) Application of microprobe
848 geochronology to hydrothermal monazite and thorite, Lemhi Pass District, Idaho.
849 *Geological Society of America Abstracts with Programs*, 34, 172.

850

851 Kamineni, D.C., and Lemire, R.J. (1991) Thorite in fault zones of a granitic pluton,
852 Atikokan, Canada: implications for nuclear fuel waste disposal. *Chemical*
853 *Geology*, 90, 133– 143.

854

855 Kosler, J., Tubrett, M., and Sylvester, P.J. (2001) Application of laser ablation ICP-MS
856 to-U-Th-Pb dating of monazite. *Geostandards Newsletter*, 25, 375-386.

857

858 Kylander-Clark, A.R.C., Hacker, B.R., and, Cottle J.M. (2013) Laser-ablation split-
859 stream ICP petrochronology. *Chemical Geology*, 345, 99–112.

860

861 Ludwig, K.R. (2003) *Isoplot/EX*, version 3. A geochronological toolkit for Microsoft
862 Excel. Berkeley Geochronology Center, Special Publication No. 4, 70 p

863

864 Mortimer, N., and Cooper, A. F. (2004) U-Pb and Sm-Nd ages from the Alpine Schist,
865 New Zealand. *New Zealand Journal of Geology and Geophysics*, 47, 21–28.

866

867 Pabst, A., and Hutton, C.O. (1951) Huttonite, a new monoclinic thorium silicate, with an
868 account on its occurrence, analysis, and properties. *American Mineralogist*, 36,
869 60-69.

870

871 Parrish, R.R., and Tirrul, R. (1989) U-Pb age of the Baltoro granite, north-west
872 Himalaya, and implications for zircon inheritance and monazite U-Pb systematics.
873 *Geology*, 17, 1076–1079.

874

875 Parslow, G.R., Brandstätter, F., Kurat, G., and Thomas, D.J. (1985) Chemical ages and
876 mobility of U and Th in anatectites of the Cree Lake zone, Saskatchewan.
877 *Canadian Mineralogist*, 23, 543-551.

878

879 Paton, C., Woodhead, J.D., Hellstrom, J.C., Hergt, J.A., Greig, A., and Mass, R. (2010)
880 Improved laser ablation U–Pb zircon geochronology through robust downhole
881 fractionation correction. *Geochemistry, Geophysics and Geosystems*, 11,
882 Q0AA06.

883

884 Searle, M.P., Noble, S.R., Cottle, J.M., Waters, D.J., Mitchell, A.H., Hlaing, T., and
885 Horstwood, M.S.A. (2007) Tectonic evolution of the Mogok metamorphic belt,

- 886 Burma (Myanmar) constrained by U-Th-Pb dating of metamorphic and magmatic
887 rocks. *Tectonics*, 26, TC3014.
- 888
- 889 Seydoux-Guillaume, A-M., Paquette, J.-L., Wiedenbeck, M., Montel, J-M.M., and
890 Heinrich, W. (2002) Experimental resetting of the U-Th-Pb systems in monazite.
891 *Chemical Geology*, 191, 165-181.
- 892
- 893 Sláma, J., Kösler, J., Condon, D.J., Crowley, J.L., Gerdes, A., Hanchar, J.M., Horstwood,
894 M.S.A., Morris, G., Nasdala, L., Norberg, N., Schaltegger, U., Schoene, B.,
895 Tubrett, M.N., and Whitehouse, M.J. (2008) Plešovice zircon—a new natural
896 reference material for U–Pb and Hf isotopic analysis. *Chemical Geology*, 249, 1–
897 35.
- 898
- 899 Speer, J.A. (1982) The actinide orthosilicates. In P.H. Ribbe, Ed. *Orthosilicates. Reviews*
900 *in Mineralogy*, 5, 67-113. . Mineralogical Society of America, Washington, DC.
- 901
- 902 Steiger, R.H., and Jäger E. (1977) Subcommittee on geochronology, convention on the
903 use of decay constants in geo- and cosmochemistry. *Earth and Planetary Science*
904 *Letters*, 36, 359–362.
- 905
- 906 Viskupic, K., and Hodges, K.V. (2001) Monazite-xenotime thermochronometry:
907 methodology and an example from the Nepalese Himalaya. *Contributions to*
908 *Mineralogy and Petrology*, 141, 233–247.

909

910 von Blanckenburg, F. (1992) Combined high-precision chronometry and geochemical
911 tracing using accessory minerals applied to the Central-Alpine Bergell intrusion
912 (central Europe), *Chemical Geology*, 100, 19-40.

913

914 Vry, J.K., Baker, J., Maas, R., Little, T.A., Grapes, R., and Dixon, M. (2004) Zoned
915 (Cretaceous and Cenozoic) garnets and the timing of high grade metamorphism,
916 Southern Alps, New Zealand. *Journal of Metamorphic Geology*, 22, 127-157.

917

918 Wendt, I., and Carl, C. (1991) The statistical distribution of the mean squared weighted
919 deviation. *Chemical Geology*, 86, 275-285.

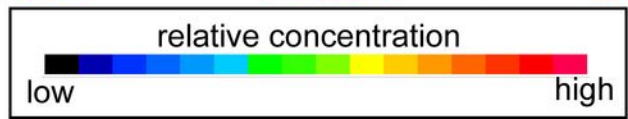
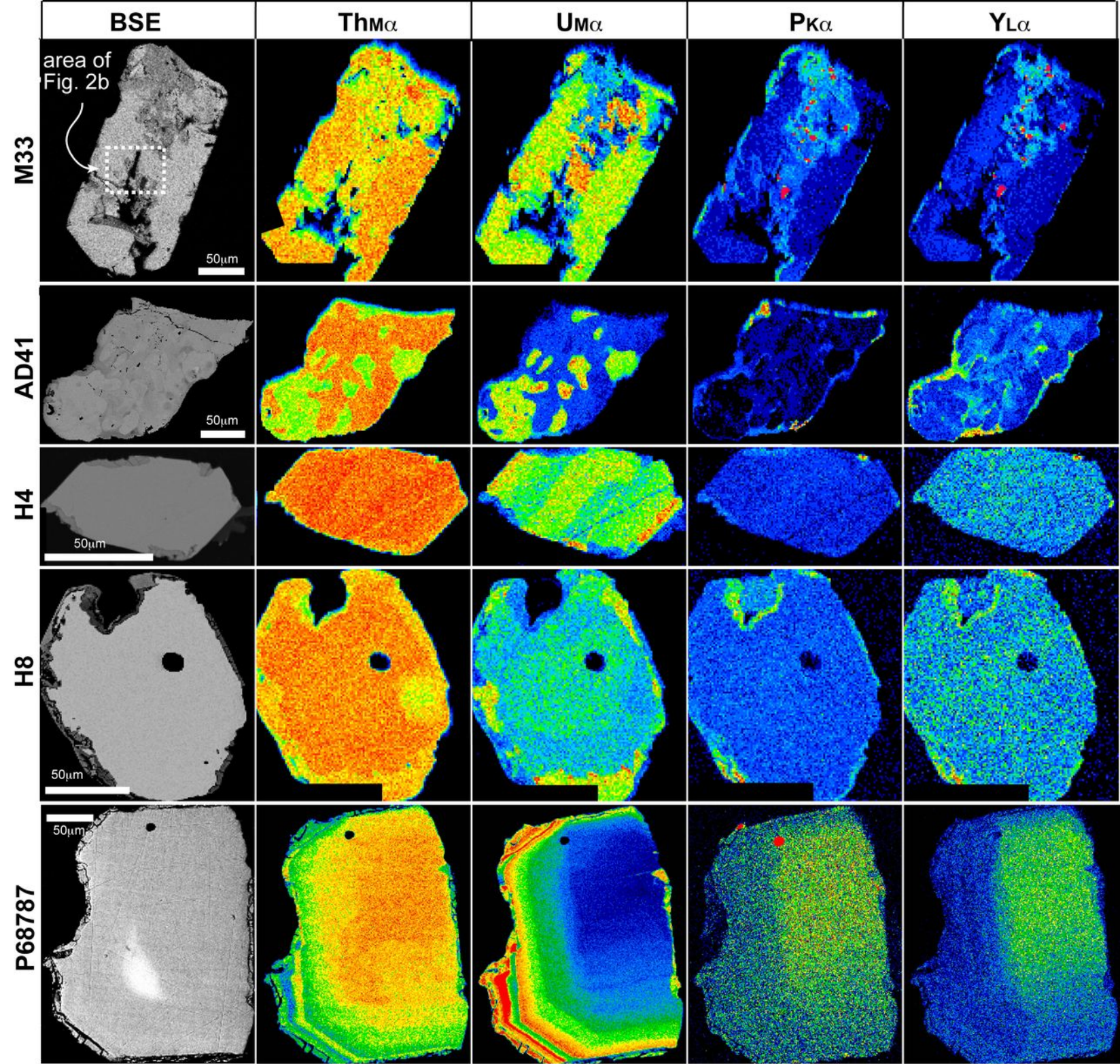
920

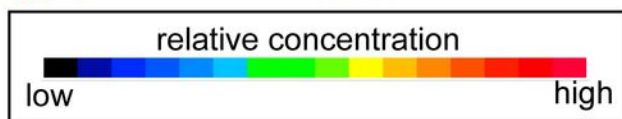
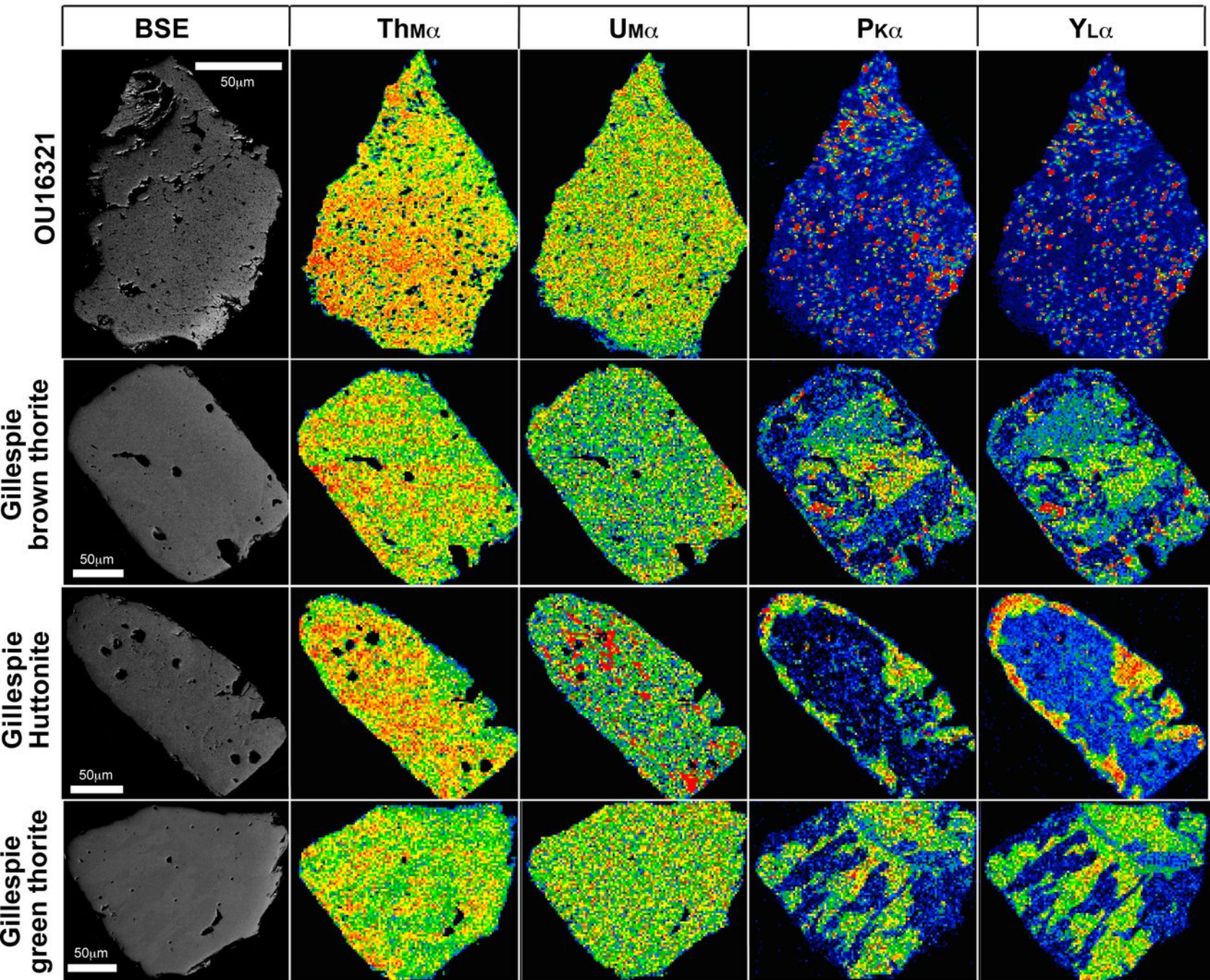
921 Whitney, D., and Evans B. (2010) Abbreviations for names of rock-forming minerals.
922 *American Mineralogist*, 95, 185–187.

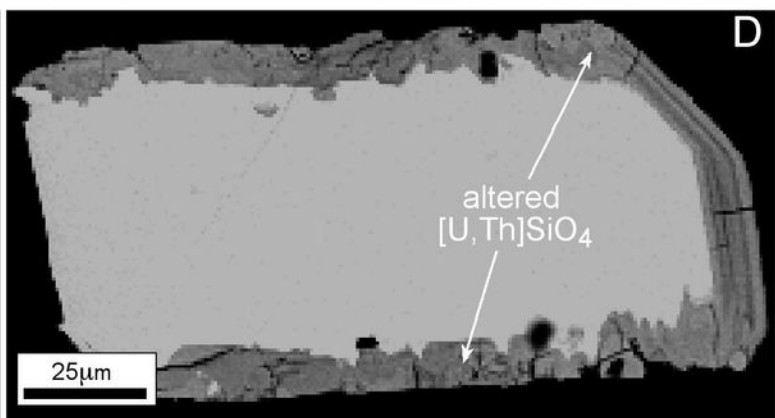
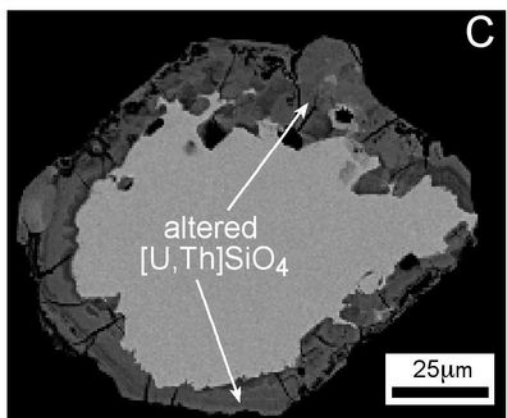
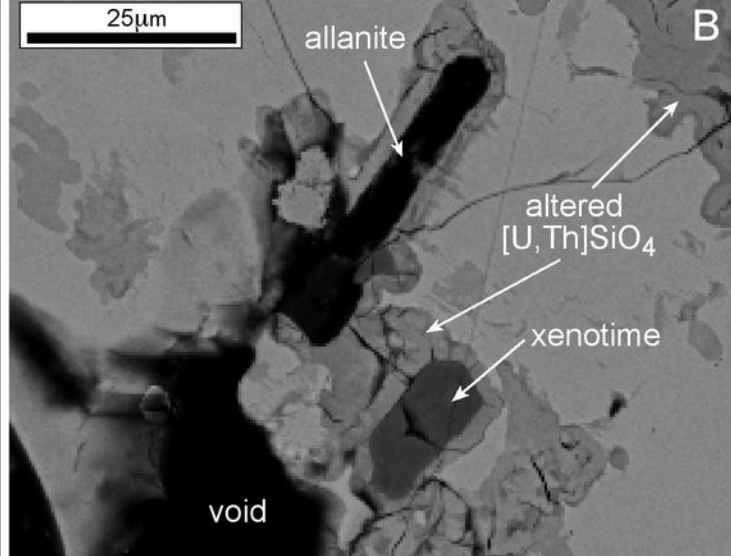
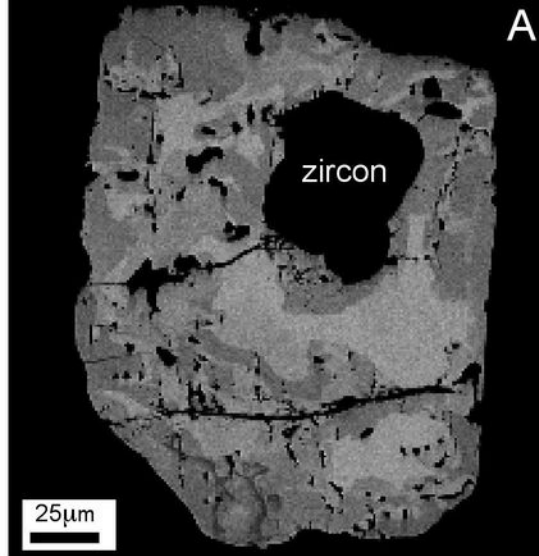
923

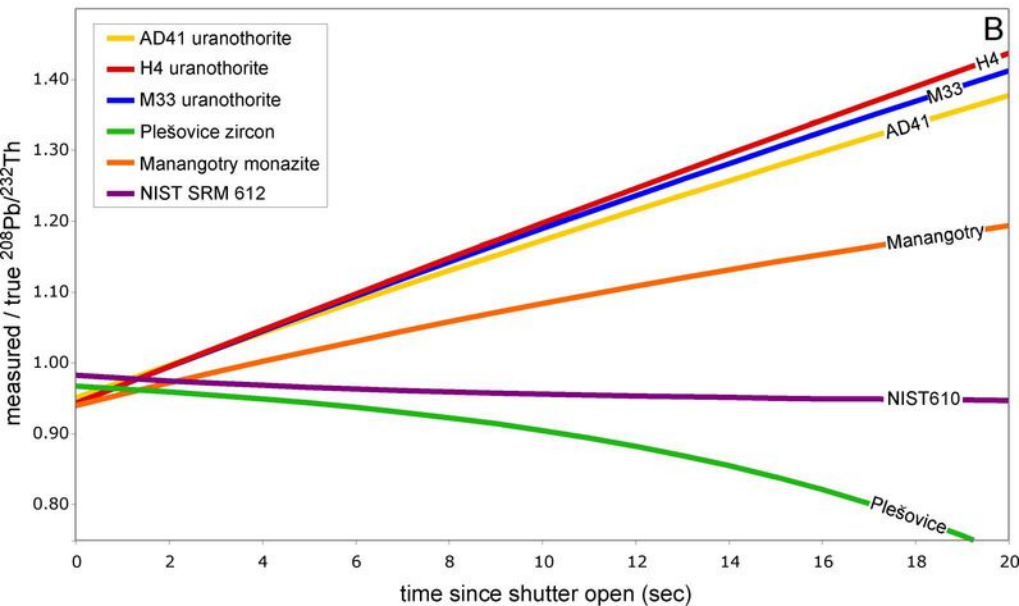
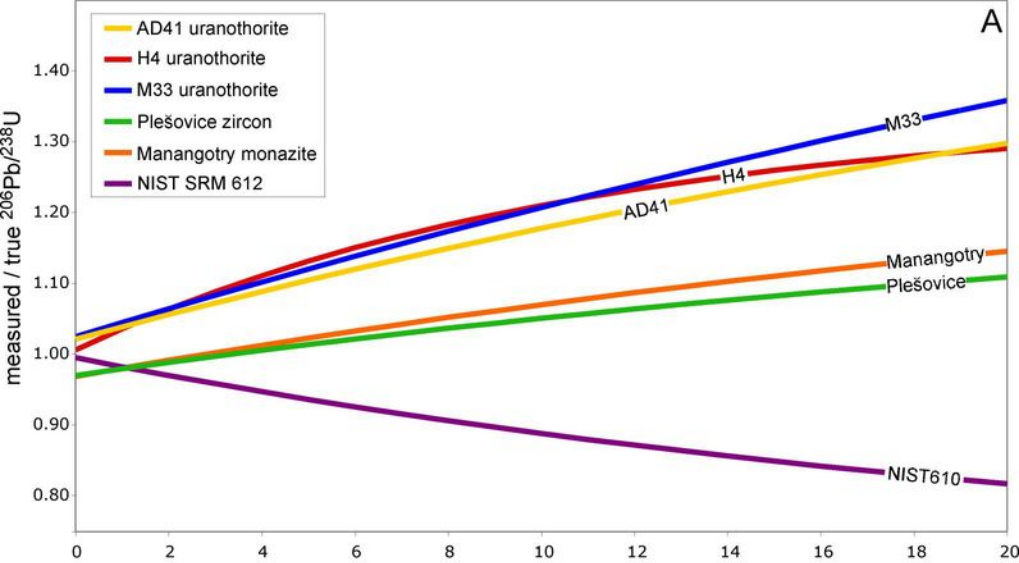
924 Wiedenbeck, M., Allé, P., Corfu, F., Griffin, W.L., Meier, M., Oberli, F., Von-Quadt, A.,
925 Roddick, J.C., and Spiegel, W. (1995) Three natural zircon standards for U–Th–
926 Pb, Lu–Hf, trace element, and REE analyses. *Geostandards Newsletter*, 19, 1–23.

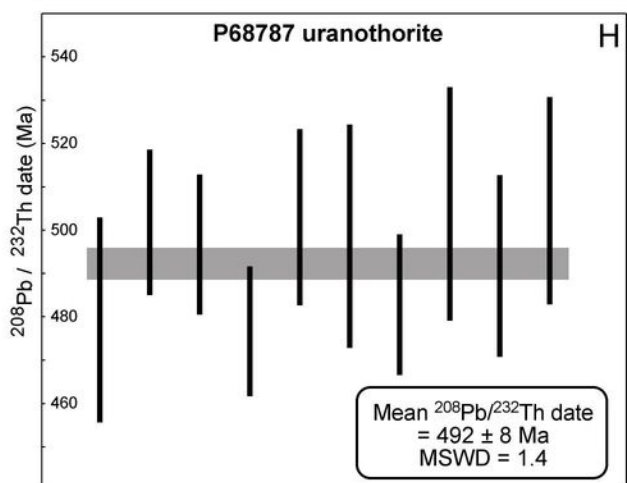
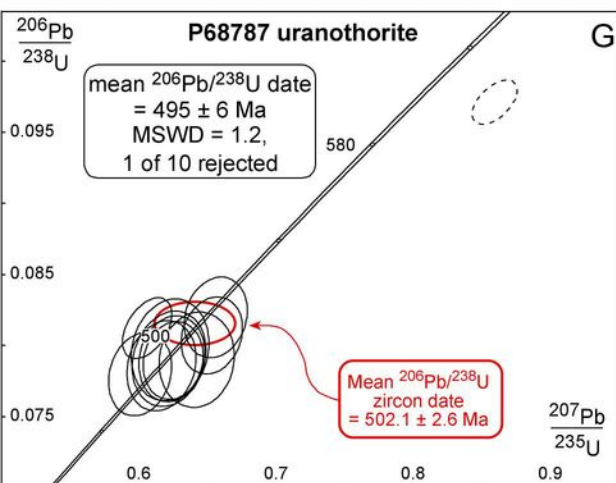
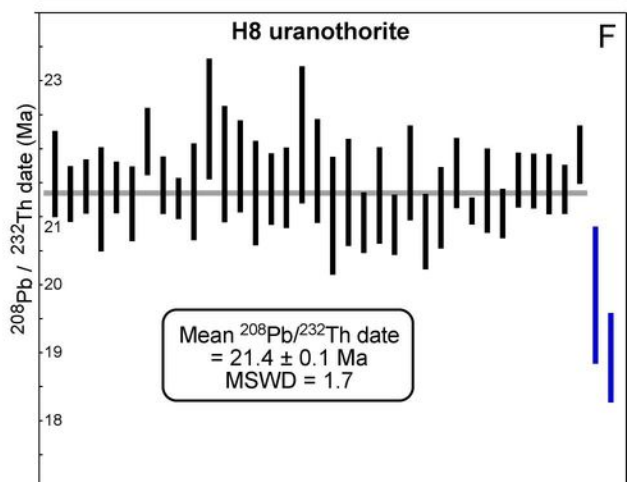
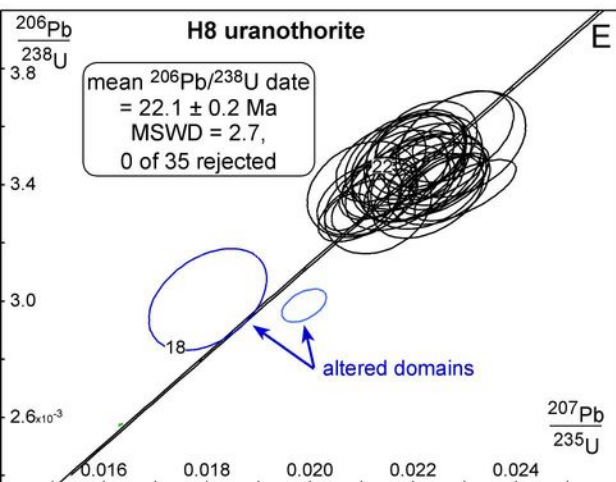
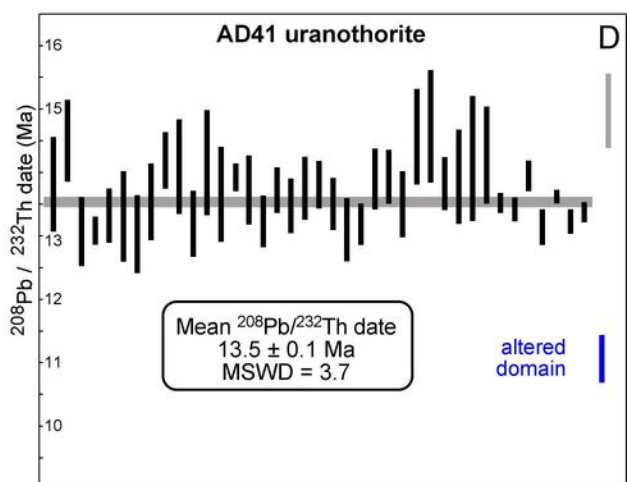
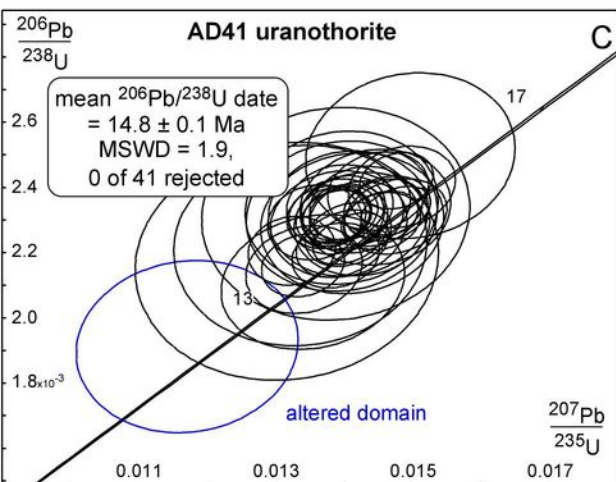
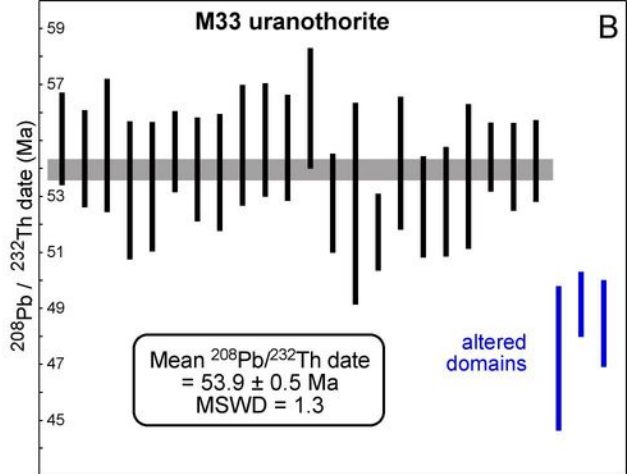
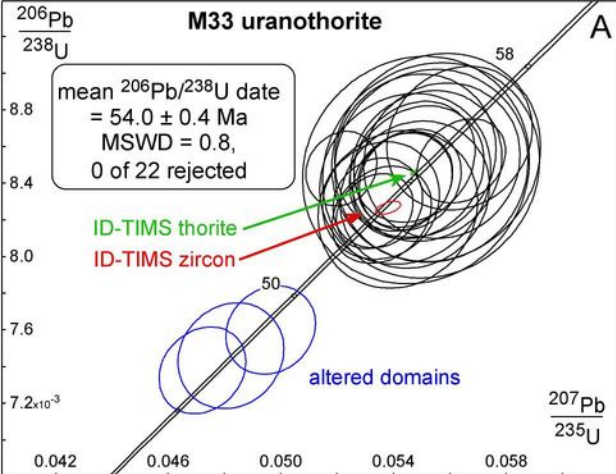
927











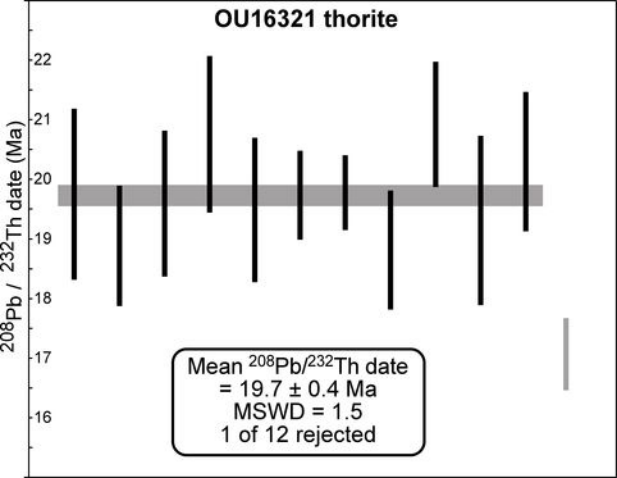
OU16321 thorite

$^{208}\text{Pb} / ^{232}\text{Th}$ date (Ma)

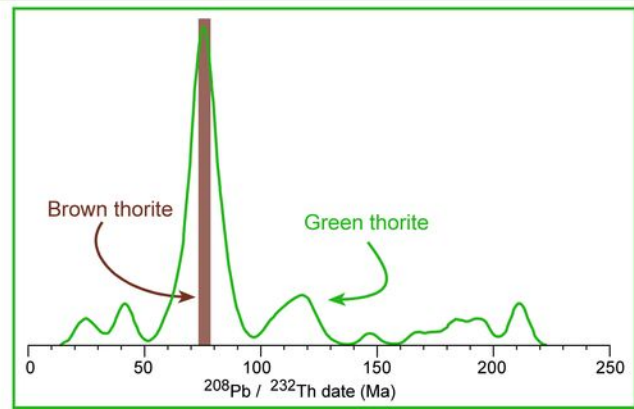
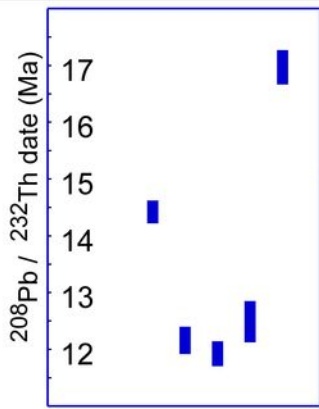
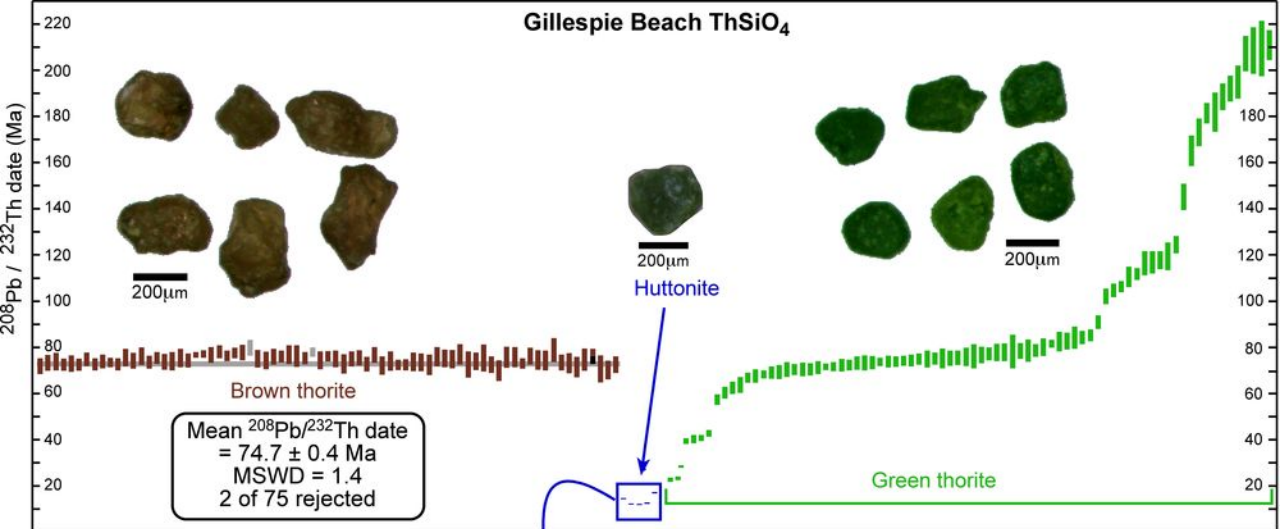
22
21
20
19
18
17
16

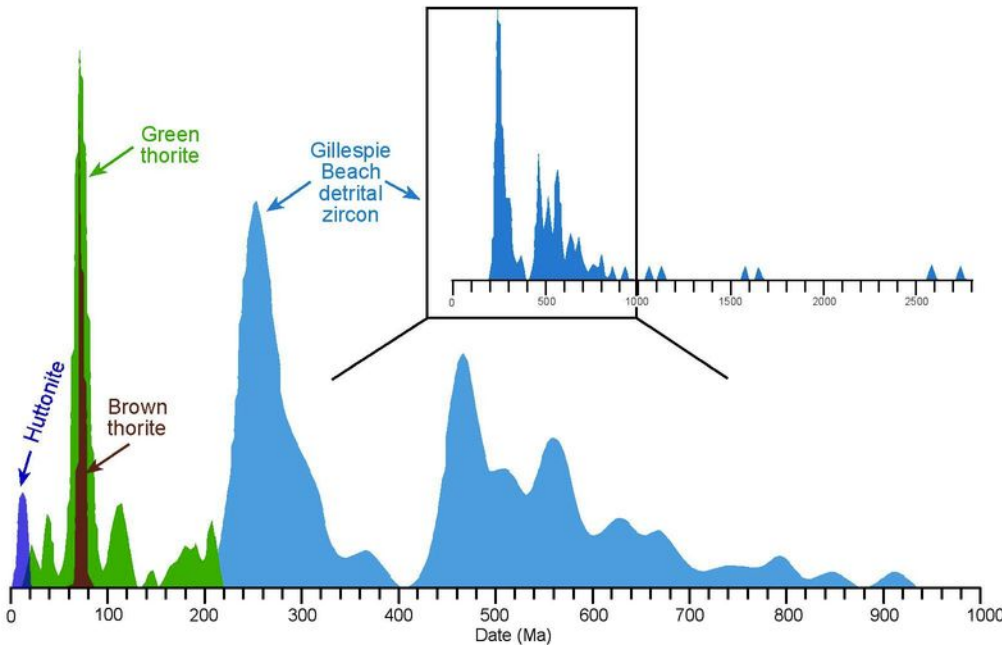
Mean $^{208}\text{Pb}/^{232}\text{Th}$ date
= 19.7 ± 0.4 Ma
MSWD = 1.5
1 of 12 rejected

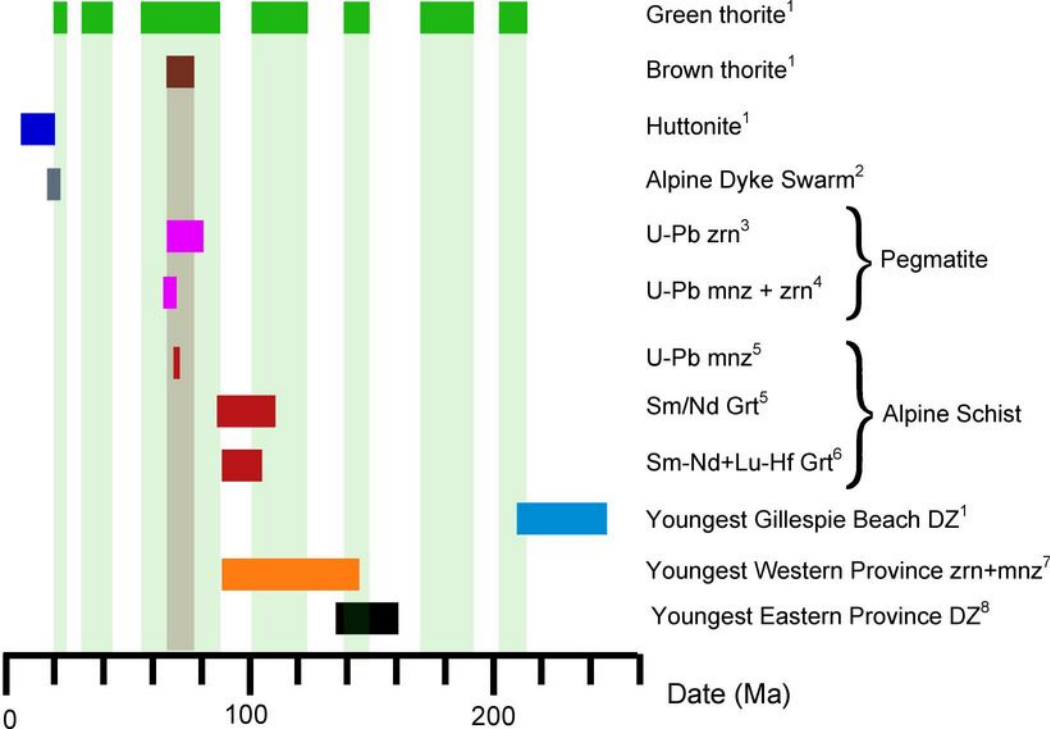
19.6



Gillespie Beach ThSiO₄







Sample	Location	sample description	Existing Date(s)	References
M33	Belin quarry, Myanmar (21.67969°, 96.14015°)	Qz+Pl+Kfs+Bt granite dike	ID-TIMS thorite: 54.1 ± 0.1 Ma LA-MC-ICPMS uranothorite: 59.5 ± 0.9 Ma	1
AD41	Kharta valley, Tibet (28.17738°, 87.35617°)	Qz+Pl+Kfs+Bt banded migmatitic augen gneiss	LA-MC-ICPMS thorite 15.8 ± 0.2 Ma	2
H4	Baltoro Glacier, Pakistan (35.7263°, 76.2878°)	monzogranite	ID-TIMS thorite: 21 Ma	3
H8	Baltoro Glacier, Pakistan (35.72176°, 76.24913°)	Kfs-megacrystic granite	ID-TIMS thorite ~16.5 Ma (discordant)	3
P68787	Hunt Glacier, Antarctica (-76.86603°, 162.34916°)	coarse-grained equigranular Hbl-monzodiorite	LA-MC-ICPMS zircon: 502.1 ± 2.6 Ma	4
OU163231	Gout Creek, New Zealand (-43.962712°, 169.29323°)	Dol+Ap+Ab+Thr+Rt carbonate-rich vein	-	5, 6, 7
Gillespie's Beach	Gillespie's Beach, New Zealand (-43.41131°, 169.79533°)	Mag+Sch+Zrn+Thr+Rt+Ap beach sand	EPMA total U-Th/Pb huttonite: 13.2 - 8.5 Ma EPMA total U-Th/Pb thorite: ~69 - 210 Ma	8, 9